



Research Paper

Mapping the Young's modulus distribution of the human tympanic membrane by microindentation

Huiyang Luo ^{a, b}, Fang Wang ^a, Chen Cheng ^a, Don U. Nakmali ^c, Rong Z. Gan ^c,
Hongbing Lu ^{a,*}

^a Department of Mechanical Engineering, The University of Texas at Dallas, Richardson, TX, 75080, USA

^b Karagozian and Case, Inc., 700 N Brand Blvd., Suite 700, Glendale, CA, 91203, USA

^c School of Aerospace and Mechanical Engineering, The University of Oklahoma, Norman, OK, 73019, USA

ARTICLE INFO

Article history:

Received 14 August 2018

Received in revised form

12 February 2019

Accepted 20 February 2019

Available online xxx

Keywords:

Human tympanic membrane
Viscoelastic
Microindentation
Young's modulus
Statistical analysis
Modulus map

ABSTRACT

The human tympanic membrane (TM, or eardrum) is composed primarily of layers of collagen fibers oriented in the radial and circumferential directions, as well as epidermal and mucosal layers at the lateral and medial surfaces. The mechanical properties of the TM depend on the microstructures of the collagen fibers, which vary with location, resulting in a spatial variation of Young's modulus. In this study, the Young's modulus of the human TM is measured using microindentation. A 10 μ m diameter spherical nanoindenter tip is used to indent the TM at different locations in the lateral and medial surfaces. Through a viscoelastic contact analysis, the steady state out-of-plane (through thickness) Young's modulus at a constant strain rate for the TM is determined from the uniaxial relaxation modulus. The measured spatial distribution of Young's modulus is reported for the entire TM pars tensa on both lateral and medial surfaces. The Young's modulus, for the four TM quadrants, is analyzed statistically using a normal quantile-quantile (Q-Q) plot. The obtained S-shaped curve indicates a bi-modal Gaussian distribution in the Q-Q plot. The spatial distribution of the Young's modulus is modeled by a bivariate Gaussian function in the polar coordinates over the entire TM on both the lateral and medial surfaces. It is shown that the anterior-superior quadrant has the smallest value of Young's modulus. Differences are observed in the spatial distribution of the Young's modulus for both the lateral and medial surfaces. For the medial surface, Young's modulus varies mainly along the radial direction following a small-large-small trend, emanating from the umbo. For the lateral surface, the modulus at the anterior-superior quadrant shows the smallest modulus; the modulus decreases gradually along the radial directions. The quantitative results presented in this paper will help improve future simulation models of the middle ear by using spatial dependence of Young's modulus over the entire TM.

© 2019 Elsevier B.V. All rights reserved.

1. Introduction

The eardrum or tympanic membrane (TM) separates the middle ear from the outer ear, and the tympanic membrane converts sound waves into vibrations of ossicular bones. The foot of the stapes converts the bone movements (vibrations) into a hydrodynamic pressure wave within the inner ear that travels along the cochlea. These traveling waves then result in deflection of the stereocilia of the cochlear hair cells and ultimately to the sensation of hearing.

However, alterations in the structures or mechanical properties of the TM due to diseases and trauma can affect the sound transmission and lead to conductive hearing loss (Gan et al., 2004, 2006 & 2010; Kochkin, 2005; Wang et al., 2007). To understand the sound transmission, it is necessary to understand the role of individual components in the middle ear in acoustic transmission (Eber and Schidhlen, 1996; Ferris and Prendergast, 2000).

Measurements of the mechanical properties over the entire eardrum provide material input parameters for finite element method (FEM) simulation models of the middle ear. Values of Young's modulus for the TM, under different conditions reported in the literature, are summarized in Table 1. The first of these measurements in 1960 reported a Young's modulus of 20 MPa for the TM using a beam test (Von Békésy, 1960). At about the same time,

* Corresponding author. Department of Mechanical Engineering, The University of Texas at Dallas, 800 W. Campbell Rd, EC38, Richardson, TX, 75080, USA.

E-mail address: hongbing.lu@utdallas.edu (H. Lu).

Abbreviations

TM	Tympanic Membrane	PI	Posterior-Inferior quadrant
Q-Q	Quantile-Quantile	U	Umbo
CDF	Cumulative Distribution Function	M	Malleus
PDF	Probability Density Function	SP	Short Process of the malleus
FEM	Finite Element Methods	TIR	Trigonum Interradiale
COD	Coefficient of Determination	C	Circumferential fiber
R ²	R squared	R ₁	radial fibers which attach straight into annular ring
LP	Lateral Process of the malleus	R ₂	a few radial fibers which diverge or crossover their terminals
AS	Anterior-Superior quadrant	T	Transverse fibers
AI	Anterior-Inferior quadrant	P	Parabolic fibers
PS	Posterior-Superior quadrant	SMR	Submucous Fine Radial fibers

the Young's modulus of TM strip was measured as 40 MPa using a longitudinal dynamic tensile oscillator (Kirikae, 1960). Later, through uniaxial tension on a human TM, the Young's modulus was determined as 23 MPa at a relatively high strain of 60% (Decraemer et al., 1980). The areal modulus of elasticity of the human eardrum was also found to depend on the undeformed area of the eardrum (Gaihede et al., 2007). The in-plane Young's relaxation modulus was determined from tensile relaxation on human TM strip specimens, primarily along the circumferential direction (Cheng et al., 2007). A nanoindentation technique was used to measure the relaxation modulus of the TM in the out-of-plane (through-thickness) direction; measurement was conducted on a small sample for demonstration of the feasibility of the technique. The in-plane Young's modulus for four quadrants of the TM was determined to be 26–38 MPa from different individuals (Huang et al., 2008). The Young's modulus of a human TM in the out-of-plane direction was found in the range of 2–15 MPa over the entire TM on the medial surface without removing the mucosal layer (Daphalapurkar et al., 2009). A human TM was stretched at high strain rates, corresponding to high frequencies up to 2000 Hz (Luo et al., 2009a & 2009b), and the Young's modulus was reported as 45–59 MPa in the radial direction, and 34–57 MPa in the circumferential direction. Using a dynamic mechanical analyzer, the storage modulus of the human TM was determined as 15–28 MPa at 1–3800 Hz using frequency-temperature superposition (Zhang and Gan, 2013).

Young's modulus values for the TM under different conditions reported in the literature are summarized in Table 1. Dynamic properties of human tympanic membrane were also measured using an electromagnetic driver to actuate remotely a magnet attached to a TM strip sample under tension (Zhang and Gan, 2010). In that work, a laser Doppler vibrometer was used to measure the

movement of the TM to determine the onset of resonance. FEM simulations were used to model the vibration of the TM strip and the dynamic stiffness at which resonance occurs. It was determined that the storage modulus was within 54–66 MPa at 200–8000 Hz. A laser holography technique was used to measure the surface profile, and motion of a tympanic membrane induced by sound (Puria, 2003; Rosowski et al., 2013; Beyea et al., 2013). A high-speed digital holography method was used to quantitatively characterize the transient dynamics of a TM (Dobrev et al., 2014). The stroboscopic holography yields maps of the amplitude and phase of the displacement of the entire membrane surface at selected frequencies (Greef et al., 2014). The measured stiffness of the TM was found to depend strongly on the fiber density in a particular portion of a TM. An indentation technique was developed to apply indentation at a particular location in an intact, full size TM, while the surface topography was measured by geometric moiré (Hesabgar et al., 2010; Aernouts et al., 2012). FEM analysis was conducted to analyze this indentation problem to determine the Young's modulus of the TM. Using this method, the Young's modulus of a rat eardrum was determined to be approximately 22 MPa, which is sensitive to the thickness of the pars tensa (Hesabgar et al., 2010). The Young's modulus of a human TM was determined through indentation; the value was found to be within 2–5 MPa (Aernouts et al., 2012). The mechanical properties of a guinea pig TM (Liang et al., 2015) and a chinchilla TM (Liang et al., 2016) were measured under pressure loading using a combined micro-fringe projection and the finite element simulation method; Young's moduli were determined as 15–28 MPa and 11–25 MPa for guinea pig and chinchilla, respectively. Since the calculation of the modulus in bulging experiments needs the thickness data as input and the thickness of a TM changes with location, using a high-

Table 1
Young's modulus values of TM reported in literature.

Literature	Young modulus (MPa) measured	Direction	Type	Methods
Von Békésy, 1960	20	Circumferential	Human	Quasi-static beam
Kirikae (1960)	40	Radial	Human	Dynamic tension
Decraemer et al. (1980)	23	Circumferential	Human	Uniaxial tension
Cheng et al. (2007).	13–22	Circumferential	Human	Tension
Huang et al. (2008)	26–38	Lateral surface	Human	Nanoindentation
Daphalapurkar et al. (2009)	2–15	Medial surface	Human	Nanoindentation
Luo et al. (2009a)	45–59	Radial	Human	SHTB
Luo et al. (2009b)	34–57	Circumferential	Human	SHTB
Zhang and Gan (2010)	54–66	Radial	Human	Dynamic tension
Zhang and Gan (2013)	15–28	Circumferential	Human	DMA
Liang et al. (2015)	15–28	Entire TM	Guinea pig	Bulging
Liang et al. (2016)	11–25	Entire TM	Chinchilla	Bulging
Hesabgar et al. (2010)	22	Local	Human	Indentation
Aernouts et al. (2012)	2–5	Entire TM	Human	Indentation

resolution optical coherence tomography apparatus, the thickness of human eardrum was found to vary between 79 and 97 μm (Kuypers et al., 2006; Jeught et al., 2013). The conventional methods for measurements of TM modulus utilize a strip or entire TM specimen; the average values for a TM are reported. However, a TM contains heterogeneous structures with possibly anisotropic behavior in the radial, circumferential, and through-thickness directions. The reported results focused on the in-plane properties; the out-of-plane properties, which could be different from the in-plane properties, were not reported for the TM. We investigate in this work the out-of-plane properties in the human TM.

In this paper, microindentation is used to probe the local indentation load-displacement response when a spherical indenter tip indents into the surface of a TM on a substrate. A viscoelastic indentation contact mechanics analysis is used to calculate the Young's relaxation modulus (Lu et al., 2003; Huang and Lu, 2006; Huang et al., 2008; Daphalapurkar et al., 2009). The measured Young's relaxation modulus is further converted into Young's modulus at a given strain rate. We report the results of Young's modulus measured on four different quadrants of a human TM, on both the lateral and medial surfaces of the human TM.

2. Materials and methods

2.1. TM structures, layout and quadrants

The human TM consists mainly of pars a tensa, surrounded by the annulus ring. A malleus bone is located in the upper half of the medial surface in the center of Fig. 1a. The pars a flaccida is located at the top. The pars a tensa contains posterior-superior (PS), anterior-superior (AS), posterior-inferior (PI), and anterior-inferior (AI) quadrants, as shown in Fig. 1a. The human TM consists of three membrane layers: the epidermal layer on the lateral surface, middle lamina propria layer, and mucosal layer on the medial surface. The lamina propria layer consists of two separate layers of bundled collagen fibers oriented in the radial and the circumferential directions (Lim, 1970 & 1995) on the lateral and medial surfaces, respectively. Fig. 1b shows a schematic diagram of these layers across the thickness (Lim, 1970; Fay et al., 2005). The mucosal layer is thin (1–2 μm , typically consists of 1–2 layers of cells) in a healthy TM. The epidermal layer is typically 8 μm thick. In order to

investigate the properties of the collagen fibrous layer, both epidermal and mucosal layers were removed during the preparation of TM samples.

2.2. Tympanic membrane samples

All TM samples used in this study were harvested from fresh-frozen human temporal bones (cadaver ears) through the Willed Body Program at the University of Oklahoma Health Science Center. The study protocol was approved by both Institutional Animal Care and Use Committees (IACUC) at the University of Oklahoma and the University of Texas at Dallas, and met the guidelines of the National Institutes of Health. The tympanic annulus was separated from the bony ear canal, while the ossicular bone chain was removed at the joints with malleus. Then, the malleus bone was removed from the TM medial surface. Since the outer epidermal and mucosal layers are much softer than the collagen fiber layers, under observation through a surgical microscope a round wooden stick (with rounded-end) was used to slightly scratch both top surfaces of TM samples for 4–5 times until the lamina propria layer was exposed; the exposed layer had no visible damage. After the outer epidermal and mucosal layers were removed, the microindenter tip was placed in direct contact with the lamina propria layer consisting of collagen fibers.

Seven (7) TM samples were prepared for the measurement on the medial surface and eight (8) TM samples were used for the measurement on the lateral surface. The TM samples were transported in a thermally-insulated cooler filled with dry ice; then stored in a freezer at -30 to -40 $^{\circ}\text{C}$ before the experiments. Each TM was defrosted for approximately 20 min prior to sectioning using a scalpel for microindentation. The information and images of the seven TM samples used for the measurement of the medial surface and the eight TM samples for measurement on the lateral surface are shown in Tables 2 and 3, respectively. Information for age, gender, and orientation (left/right) is also shown in both tables for each TM.

2.3. Microindentation experiments

Since a TM is a nearly conical-shaped membrane with a cone angle within 132° – 137° (Gaihede et al., 2007), it is not possible to

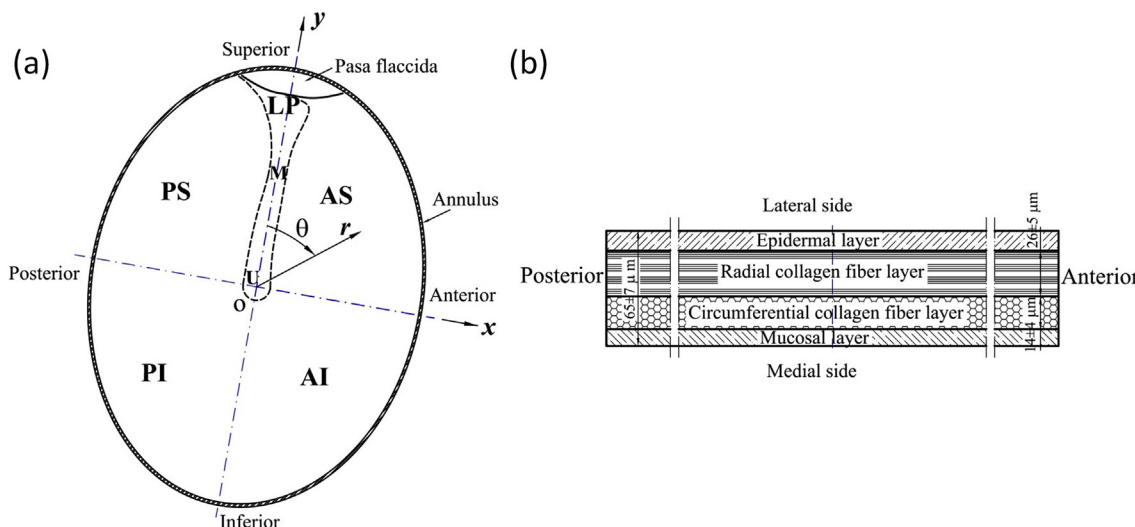


Fig. 1. Schematic diagram of human TM layout and structures.(a). Four quadrants of right ear TM at lateral view (Beyea et al., 2013). LP: lateral process of the malleus, AS: Anterior-Superior quadrant, AI: Anterior-Inferior quadrant, PS: Posterior-Superior quadrant, PI: Posterior-Inferior quadrant; U: Umbo, M: Malleus; (b). Schematic of TM layer structure (Fay et al., 2005; Daphalapurkar et al., 2009).

Table 2

Information on the 7 TMs for microindentation on the medial surface.

Sample	TB08-02	TB08-03	TB08-17	TB08-27	TB08-28	^a TB09-05	TB09-08
Image							
Information Data points	89/M/R 82	83/F/L 83	77/F/L 77	71/F/L 74	71/F/R 84	60/M/L 97	60/F/R 89

Notation: M – Male, F – Female, R – Right ear, L – Left ear.

Note:

^a TB09-05 TM sample was dyed with biocompatible blue pigments for other testing. Since the pigments are ultramarine nanoparticle with diameters in tens of nanometers, soluble to water and dispersed in solution with less than 1% w/w concentration, the dye is not anticipated to significantly affect the TM mechanical properties such as modulus results. The total number of indentations made on these samples is 586.

Table 3

Information on the 8 TMs for microindentation on the lateral surface.

Sample	^a TB09-19	TB09-20	TB10-01	TB10-02	TB10-03	TB10-22	^b TB10-23	TB10-24
Image								
Information Data points	66/M/L 41	66/M/R 73	59/F/L 78	59/F/R 108	80/M/L 98	87/F/R 77	74/F/L 113	74/F/R 110

Note:

^a Only half of TB09-19 TM was harvested.

^b TB10-23 TM was already cut into four quadrants for microindentation testing. The total number of indentations made was 698. The small grids at the bottom of each image show a scale bar with the side length of each grid at 1.0 mm.

lay down an entire TM flat on a substrate. Thus, to obtain a flat specimen for the microindentation experiments, a TM was cut into four quadrants, which were then laid down flat on an aluminum substrate. A quadrant of the TM sample was placed on the aluminum substrate. Before microindentation, each TM specimen was gently stretched by several cycles on a flat substrate for preconditioning and flattened gently before placing it on the aluminum substrate. This process is not anticipated to damage the collagen fiber network of the TM sample (Cheng et al., 2007; Daphalapurkar et al., 2009). The TM initially placed on the aluminum substrate was soaked in saline solution (0.9% NaCl, pH 5.6). Fingers covered with a silicone rubber glove gently pressed a quadrant against the hard substrate, to allow the TM quadrant to stay flat and rest on the substrate, to ensure that no air was entrapped between the TM sample and the substrate. The force applied was estimated to be in the neighborhood of 0.1 N, and was not anticipated to induce damage to the collagen fiber network of the TM sample. The saline solution allowed its meniscus to make contact with the TM periphery, so that the TM remained in the moisturized condition during microindentation. The same round wooden sticks were used to flip the TM sample, and to stretch and flatten the TM sample gently for 3–4 times for preconditioning.

A schematic diagram of a sample mounted on a specimen holder (island) for microindentation is shown in Fig. 2a. The circular groove surrounding the island was filled with saline solution to allow the saline solution to moisturize the TM sample during microindentation. An actual AI quadrant placed on an island substrate in the center is shown in Fig. 2b. An entire TM that was cut to four quadrants is shown in Fig. 2c, before placement on the aluminum island substrate. During microindentation, the saline level was monitored and the saline solution was added every 10 min, to ensure that the TM was maintained in a saline-soaked condition. Microindentation was made on either the medial surface or the lateral surface in all measurements. Within the TM, the

collagen fibers are aligned either along the radial direction on the lateral surface or in the circumferential direction on the medial surface, as observed by high-magnification SEM images (Moller, 1981, 1984; Cheng, 2007; Mota et al., 2015).

The TM is a thin membrane of material in a rubbery state. Its lateral surface is in contact with air, and *in-vivo* its periphery has only the annulus ring connected to the ear canal tissue at the body temperature of 37 °C. Under this situation, the TM temperature is likely to be between room temperature and the body temperature. Therefore, it seemed feasible to conduct the microindentation experiments at approximately 23 °C.

The long time it took for microindentation on a TM quadrant made it difficult to perform testing on both sides of each sample. Specifically, one microindentation site was conducted in 30 min. This process includes identification of contact point (5 min), loading and unloading (10 min), and thermal drift correction for the nanoindenter system (15 min). Each TM quadrant had 20–30 microindentation sites and it took about 10–15 h to complete the microindentation experiments on one quadrant. After this long time on one surface, the same TM was no longer suitable for another 10–15 h of microindentation on the other surface. Therefore, microindentations were made on only one of the two surfaces of each sample.

Microindentation was made on each quadrant of TM, starting from the inner location close to the umbo towards the outer perimeter along radial directions. The umbo is set as the origin, and the indents close to umbo were nearly evenly distributed along the radial lines. For each quadrant, microindentation was made along 3–6 different radial lines; along each radial line, microindentation was made at about 10 locations. The microindentation point array is along the radial direction, with an angle of 20° of separation from a neighboring array. The first array of microindentation points form an angle of 10–15° from the cutting edge. The location of each microindentation point is controlled by a positioning stage with submicron resolution. The location of the umbo center was taken as

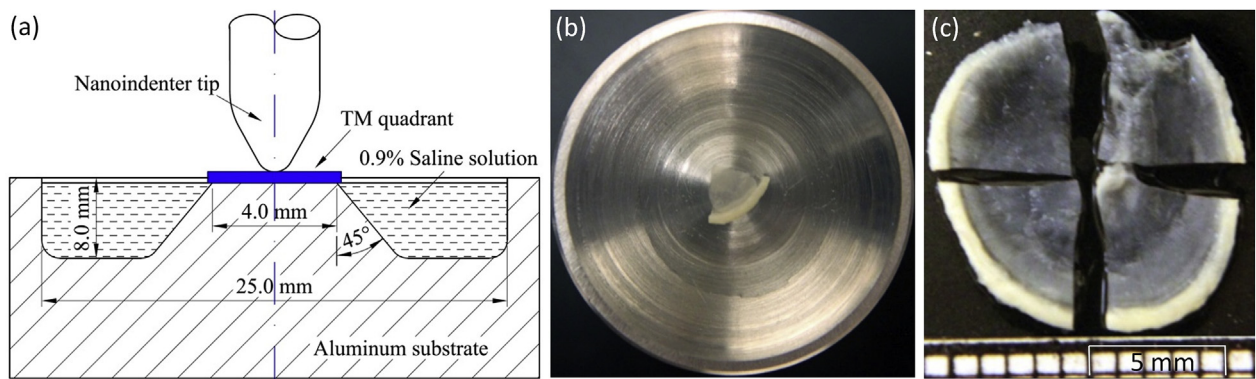


Fig. 2. Through-thickness microindentation experimental setup.(a). Schematic setup;(b). An actual top view of Al quadrant TM placed on an aluminum substrate;(c). Image of four cut TM quadrants (TB10-24).

the origin, and one cutting edge was selected as the *x*-direction. A small amount of shrinkage (5–10%) of collagen fibers in the cutting section (at the cutting edge) occurred and is considered to have negligible effect on the property measurements on locations far away from the edges, and microindentations were made at points far away from the cutting edge. In [Tables 2 and 3](#), the total number of microindentation points is also given for each TM sample. The actual shapes of the manubrium of each TM are also shown in [Tables 2 and 3](#). In total, 586 and 698 microindentations were made in the medial surface and the lateral surface, respectively. In [Fig. 3a](#), a schematic drawing on these measurement points on the Al quadrant is shown as an example.

Microindentation was conducted on four quadrants of the TM and the Young's modulus results are reported. To determine the spatial distribution of Young's modulus, under the nanoindenter tip (10 μm radius), the indent impression would have a dimension on the order of 10 μm at an indentation depth of 1.2 μm ; hence, there are many collagen fibers (each collagen fiber has approximately 10 nm diameter) within the indent impression. Thus, for analysis, the continuum assumption is made to determine the local effective properties.

2.4. Viscoelastic analysis

The microindentation depth is on the order of a few microns, which is less than 1/10 of the thickness of the TM (70 μm). Therefore, the spherical indentation into the TM sample is modeled as a contact mechanics problem in which a sphere indents into a viscoelastic half space ([Lu et al., 2003, 2006; Huang and Lu, 2006; Huang et al., 2008](#)). The diamond indenter tip has a modulus that is four orders of magnitude higher than that of the TM, so that the tip is modeled as rigid. From Hertzian contact mechanics analysis, with the consideration of a time-dependent viscoelastic boundary value problem ([Lee and Radok, 1960](#)), the viscoelastic microindentation depth, $h(t)$, is calculated from the microindentation load, $P(t)$, using the following equation ([Lu et al., 2003](#)):

$$h^{3/2}(t) = \frac{3(1-\nu)}{8\sqrt{R}} \int_{-\infty}^t D(t-\xi) \left[\frac{dP(\xi)}{d\xi} \right] d\xi \quad (1)$$

where ν is the Poisson's ratio, assumed to be constant, R is the radius of the spherical indenter, $D(t)$ is the uniaxial creep

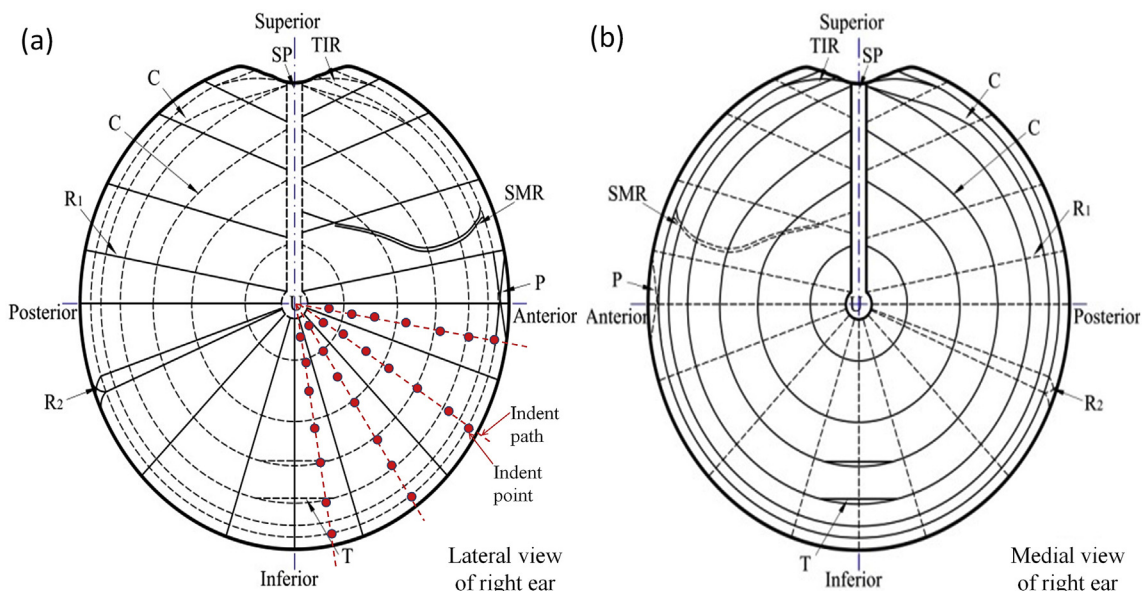


Fig. 3. A schematic diagram showing fiber orientations in a human tympanic membrane of right ear (adapted from [Lim, 1995](#)). (a). Lateral view; (b). Medial view. Note, in (a), a schematic of indent path (4 radial lines separated by about 20°) and indentation points (about 7 points) are marked in red dash-lines and dots in Al quadrant, respectively. SP: short process of the malleus; TIR: trigonum interradiale; C: circular fiber; R₁: radial fibers which attach straight into annular ring; R₂: a few radial fibers which diverge or crossover their terminals; T: transverse fiber; P: parabolic fibers; SMR: submucous fine radial fiber.

compliance. A curve fitting approach is used to determine the creep compliance. In this method, the uniaxial creep compliance is represented as a generalized Kelvin model,

$$D(t) = D_0 + \sum_{i=1}^N D_i \left(1 - e^{-t/\tau_i}\right) \quad (2)$$

where D_0 and D_i ($i = 1, \dots, N$) are compliance coefficients, τ_i are retardation times, N is the number of terms in the Prony's series. For spherical microindentation under a constant rate loading history, $P(t) = P_0 t H(t)$, where P_0 is the constant loading rate, and $H(t)$ is the Heaviside unit step function, substituting Eqn. (2) into Eqn. (1) leads to:

$$h^{3/2}(t) = \frac{3(1-\nu)}{8\sqrt{R}} \left[\left(D_0 + \sum_{i=1}^N D_i \right) P(t) - \sum_{i=1}^N D_i (v_0 \tau_i) \left(1 - e^{-\frac{P(t)}{v_0 \tau_i}}\right) \right] \quad (3)$$

The loading rate $P_0 = 8.83 \mu\text{N/s}$ was applied in this study. This value is the same as that used in our previous microindentation measurements on TM (Huang et al., 2008; Daphalapurkar et al., 2009). Since the viscoelastic theory was used to convert the relaxation modulus to Young's modulus at a given strain rate, the effect of loading rate has been considered in the analysis. However, it does not play an additional role in the interpretation of the measurement results.

Using the least squares correlation to fit Eqn. (3) to the load-displacement curve measured from microindentation, all parameters, D_0 , D_i , and τ_i are obtained. With the known parameters, the creep compliance in Eqn. (2) is determined. The relaxation modulus $E(t)$ is obtained from the uniaxial creep compliance (Knauss et al., 2008) by:

$$\int_0^t E(\tau) D(t-\tau) d\tau = t \quad (4)$$

Since TM is a soft tissue in its rubbery state, its Poisson's ratio is usually taken as 0.495 to avoid an ill-posed problem. The relaxation modulus was determined numerically from the uniaxial creep compliance using an inversion method (Luo et al., 2013). The discrete relaxation modulus data is subsequently fitted with a generalized Maxwell model:

$$E(t) = E_\infty + \sum_{i=0}^N E_i e^{-t/\tau_i} \quad (5)$$

where E_∞ is the steady-state relaxation modulus, E_i ($i = 0, \dots, N$) are relaxation coefficients.

Since the TM behaves as nearly linearly viscoelastic at small deformations (Luo et al., 2009a; 2009b), using a linearly viscoelastic analysis, the Young's relaxation modulus can be converted into Young's modulus at a given strain rate (Luo et al., 2010, 2013). For a linearly viscoelastic material under uniaxial stress state, the uniaxial stress $\sigma(t)$ is calculated from the applied strain history $\epsilon(t)$, using the Boltzmann superposition principle:

$$\sigma(t) = \int_0^t E(t-\xi) \frac{d\epsilon(\xi)}{d\xi} d\xi \quad (6)$$

where $E(t)$ is the Young's relaxation modulus. At a constant strain rate $\dot{\epsilon}_0$, $\epsilon(t) = \dot{\epsilon}_0 t$, Eqn. (6) becomes:

$$\bar{E}(t) = \frac{\sigma(t)}{\dot{\epsilon}(t)} = \frac{1}{t_0} \int_0^{t_0} E(\xi) d\xi \quad (7)$$

where $\bar{E}(t)$ is the average uniaxial relaxation modulus from time 0 to t_0 . Eqn. (7) indicates that the average Young's relaxation modulus (over time period 0 to t_0) is equal to the Young's modulus at a constant strain rate $\dot{\epsilon}_0$ (Luo et al., 2009a; 2009b, 2010, 2013).

2.5. Young's modulus map

Since different TMs have different dimensions and shapes, the dimensions are normalized for comparison of modulus data obtained from different locations of individual TMs. Since most TMs have either round or elliptical shape, the locations are normalized by dividing the radial coordinate by the diameter (r_0 for round shape) or the length of the major axis (for elliptical shape). The actual Cartesian coordinates (x' , y') are converted into the normalized Cartesian coordinates (x , y) through $x = x'/r_0$ and $y = y'/r_0$, with a range $[-1, 1]$, with the umbo center as the origin (0, 0). The normalized Cartesian coordinates x - y are further converted into polar coordinates (r, θ) through:

$$r = \sqrt{x^2 + y^2}, \quad \theta = \tan^{-1}\left(\frac{y}{x}\right) \quad (8)$$

where $-1 \leq x, y \leq 1$, $0 \leq r \leq 1$, $0^\circ \leq \theta \leq 360^\circ$. Fig. 1a shows the coordinate conversion. At the malleus, $\theta = 0^\circ$, and θ is positive in the clockwise direction. After normalization into polar coordinates, all modulus data are combined and plotted as a Young's modulus map.

Since a TM has four views: lateral view at right ear, medial view at right ear, lateral view at left ear, and medial view at left ear, three views are transformed onto the lateral view in the right ear as shown in Fig. 3a. It has the same configuration as the medial view at the left ear. They are symmetric with respect to other two views (lateral surface at left ear, and medial surface at right ear) with respect to the malleus bone axis. Therefore, all other three views projected onto the lateral view in the right ear are unique for identification of the location for the comparison.

2.6. Statistical analysis

2.6.1. Q-Q plot

In this statistical analysis, the first step is to construct a histogram from the experimental data. A quantile-quantile (Q-Q) plot is used to evaluate visually the data set. The Q-Q plot (or probability plot) gives a quick graphical diagnostic on whether the experimental data follows the assumed distribution or not (Chambers et al., 1983). It is noted that the location information is not considered in this Q-Q plot analysis. Instead, the spatial dependence is considered in the modeling of the modulus distribution described in the next section.

The procedures to construct the Q-Q plot are given as follows (Chambers et al., 1983):

- Sorting data: The experimental data set $\{x_1, x_2, \dots, x_i, \dots, x_n\}$ for $i = 1, 2, \dots, n$, is sorted from the lowest to the highest values. The sorted values are denoted by $\{x_{(1)}, x_{(2)}, \dots, x_{(i)}, \dots, x_{(n)}\}$, where $x_{(1)} < x_{(2)} < \dots < x_{(i)} < \dots < x_{(n)}$. The subscripts in parentheses represent the new resorted order for $(i) = (1), (2), \dots, (n)$.
- Calculating the experimental accumulated probability q_i : The values at $x_{(i)}$ are used to calculate this value:

$$q_i = \frac{i - 0.5}{n} \quad (i = 1, 2, \dots, n) \quad (9)$$

(c). Calculating the theoretical quantile: Since the cumulative distribution function (CDF), $\Phi(z)$, has an integration relation with the probability density function (PDF) $\phi(z)$, $\Phi(z)$ is calculated as:

$$\Phi(z) = \int_0^z \phi(\xi) d\xi \quad (10)$$

The quantile notation is used. If z_i is the i th quantile of a distribution, then $\Phi(z_i) = q_i$. Thus, the theoretical quantile is defined by the inverse function of the CDF as

$$z_i = \Phi^{-1}(q_i) \quad (11)$$

(d). Q-Q plot: The sorted experimental quantile set of $\{x_{(i)}\}$ is plotted as the abscissa and the theoretical quantile set of $\{z_i\}$ is plotted as the ordinate, to form the Q-Q plot.

2.6.2. PDF and CDF plots

Through Q-Q plots, the Young's modulus data from human TM is tested to determine whether it follows a single-modal or multi-modal normal distribution. At the same time, the histogram and the empirical CDF figure are constructed. In the histogram, the sorted experimental quantile data set of $\{x_{(i)}\}$ ($i = 1, 2, \dots, n$) is used as the abscissa. Then, the ordinate represents the empirical probability density $\phi'(x_i)$, calculated from the relative frequency f_i divided by the empirical quantile step:

$$\phi'(x_i) = f_i / [(x_{(n)} - x_{(1)})/n] \quad (12)$$

where the relative frequency f_i is defined as the ratio of counts occurring in the interval (x_i, x_{i+1}) to that of the total counts. Therefore, the bar figure with sorted data set $\{x_{(i)}\}$ and the empirical probability density are plotted as the histogram (PDF plot). For the empirical CDF figure, the abscissa is the sorted experimental quantile set of $\{x_{(i)}\}$ ($i = 1, 2, \dots, n$), and the ordinate is the accumulated probability, or the calculated experimental accumulation $\{q_i\}$. The data set of $\{x_{(i)}, q_i\}$ is then plotted as the empirical CDF figure and is used for comparison between modeling results and the experimental data to determine the distribution parameters.

2.6.3. Modeling the modulus map

The Young's modulus of human TM changes with location as indicated by microindentation measurement; the modulus depends on the fiber arrangements. Fig. 3a shows the conceptual fiber arrangements for human tympanic membrane (adapted from Lim, 1995) of the right ear. In addition to the major radial and circumferential collagen fibers, R₁, R₂, T, P, and SMR, fibers also exist in a TM either on the medial or lateral surface. Fig. 3b for the medial surface shows a pattern, similar to the lateral surface, except with a different orientation. It is nearly a mirror image of Fig. 3a with respect to the malleus bone axis. The solid lines represent the fibers at the top, and the dashed lines refer to the hidden fibers below the surface layer. The other two views of TMs in the left ear have similar patterns to those of the right ear, at different orientations. With a projection onto the lateral view in the right ear, all modulus results are presented in the sequel for comparison. With all this data

available, it is possible to model the statistical distribution of Young's modulus.

In general, for the multi-modal Gaussian distribution, the probability density function is the summation of individual Gaussian PDFs weighted by factors, given as:

$$g(E) = \sum_{i=1}^N \frac{\alpha_i}{\sigma_i \sqrt{2\pi}} e^{-\left[0.5\left(\frac{E-\mu_i}{\sigma_i}\right)^2\right]}, \quad (13)$$

where N is the order of multi-modes, α_i , σ_i , μ_i ($i = 1$ to N) are the weight factors ($\sum_{i=1}^N \alpha_i = 1$), the standard deviation and expectation (mean) values, respectively. The corresponding CDF is given as:

$$G(E) = 0.5 + 0.5 \sum_{i=1}^N \alpha_i * \text{erf}\left(\frac{E - \mu_i}{\sigma_i}\right), \quad (14)$$

where erf is the error function. When a bimodal Gaussian function is chosen, the order is $N = 2$. The best-fit parameters α_i , σ_i , μ_i ($i = 1, 2$) are determined using the nonlinear least squares Levenberg-Marquardt method (Luo et al., 2015; Xu et al., 2018). With these parameters known, the theoretical multi-Gaussian PDF curve was constructed, and compared with the experimental histogram.

3. Results and discussion

3.1. TM samples and microindentation

The information and images for the TM samples are shown in Tables 2 and 3. It is noted that portions of some annulus rings are damaged during preparation of the TM samples. Since micro-indentation is made on the pars tensa, the damage in the annulus ring does not affect the TM modulus measurement. The left/right ear orientation listed is important for projection of TMs at different surfaces and orientations onto the same lateral view in the right ear, so that the combined modulus data from different TMs can be analyzed for further comparison.

The mechanical properties determined represent those of the lamina propria. The maximum indentation depth used for viscoelastic analysis to determine viscoelastic properties (Lu et al., 2006) is restricted to $1.2 \mu\text{m}$ so that the effect of substrate can be neglected since the maximum indentation depth was less than $1/35$ of the TM thickness. The microindentation load-displacement curve is very similar to previous work on the human TM (Huang et al., 2008; Daphalapurkar et al., 2009). A typical micro-indentation load-displacement curve is shown in Fig. 4, with labels indicating the loading and unloading paths. The Young's modulus is calculated from the loading curve.

In any quadrant of the TM, collagen fibers are largely oriented within a plane. The TM quadrant could be considered as a transversely isotropic material. The Young's modulus in the through-thickness direction can be different from the in-plane modulus. The relaxation functions were obtained based on the analysis of a homogeneous, isotropic, linearly viscoelastic material. The nano-indentation in the through-thickness direction invokes primarily the behavior of the material in the thickness direction (Daphalapurkar et al., 2009). The assumption of isotropy in this analysis is not anticipated to affect the measurement of the through-thickness Young's relaxation modulus significantly (Daphalapurkar et al., 2009).

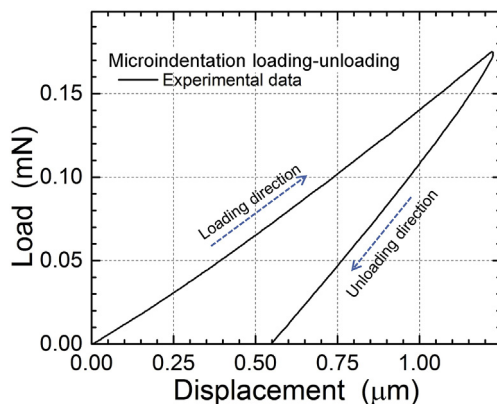


Fig. 4. Typical microindentation load-displacement curve for human TM.

3.2. Young's modulus map

A typical Young's modulus map at the medial surface in the normalized (x, y) coordinate system for the TM sample TB 08-02 is shown in Fig. 5a. It is noted that the original Young's modulus map in the actual (x', y') coordinate system has the same map as shown in Fig. 5a, the difference is in the coordinate scales used. After the rectilinear coordinates (x, y) are converted into the polar coordinates (r, θ), the Young's modulus map has a symmetric configuration with respect to the y -axis. For the right ear with microindentation at the medial surface, the medial view is shown in Fig. 5a and the lateral view is shown in Fig. 5b. The small black dots in the polar coordinates show the actual locations of micro-indentation. The original modulus maps (Fig. 5a) show an irregular boundary formed by piecewise lines connecting neighboring points at the actual boundary. The boundary is within the TM pars a tensa range, close to the annulus ring. The maps in the polar coordinates (Fig. 5b) show a smooth round boundary at $r = 1.0$, defined as the dimensionless radial coordinate, which is the ratio of the radius of a point to the radius of the annulus. The data at the boundary is interpolated. The Young's modulus maps for the other six TMs

measured at the medial surface (TB08-03, TB08-17, TB08-27, TB 08-28, TB09-05 and TB09-08) are shown in the lateral view of Fig. 6a-f in the normalized polar coordinates.

Another typical Young's modulus map of TM at the lateral surface is shown in Fig. 7 for the TM sample labeled TB10-02. Fig. 7a is plotted with the same configuration as Fig. 7b at the same lateral view of right ear. Fig. 8a-f (the lateral view) show the Young's modulus maps for the lateral surface for six TMs: TB09-20, TB10-01, TB10-03, TB10-22, TB10-23 and TB10-24, except for TB09-19, which has results for only a half of the TM.

In Figs. 5-8, the Young's modulus data shows one or more peaks, where the locations and values vary with different TMs. In order to find common features, all modulus data from different TMs are combined into a single modulus map from all seven TM samples at the medial surface and all eight TMs at the lateral surface, respectively.

We define the coordinates of each point in Fig. 1a and convert the map of four quadrants into a combined map for each TM. Figs. 5b, 6 and 7b and 8 show the smooth interpolated 2D map in polar coordinates. Even though microindentation on each TM has low spatial resolution and different distribution, combining all data from different TMs, a trend and distribution are obtained through statistical analysis. The results are analyzed statistically in Section 3.3, and the modulus map is modeled based on the statistical analysis. These results show effective properties for the TMs used in this study.

3.3. Normal Q-Q plot

A normal Q-Q plot is used to test whether the modulus distribution follows a single-modal or multi-modal normal distribution. This plot compares the experimental quantiles against a corresponding theoretical fitted quantiles. The normal (Gaussian) distribution is assumed as the theoretical reference. It is represented as $N[\mu, \sigma]$, with mean μ and standard deviation σ . Consequently, the normal probability (or normal Q-Q) plot provides a quick test for the null hypothesis that the data follows a normal distribution (Filliben, 1975; Gnanadesikan, 1977). If the points in the Q-Q plot fall approximately on a straight line, the hypothesis is supported.

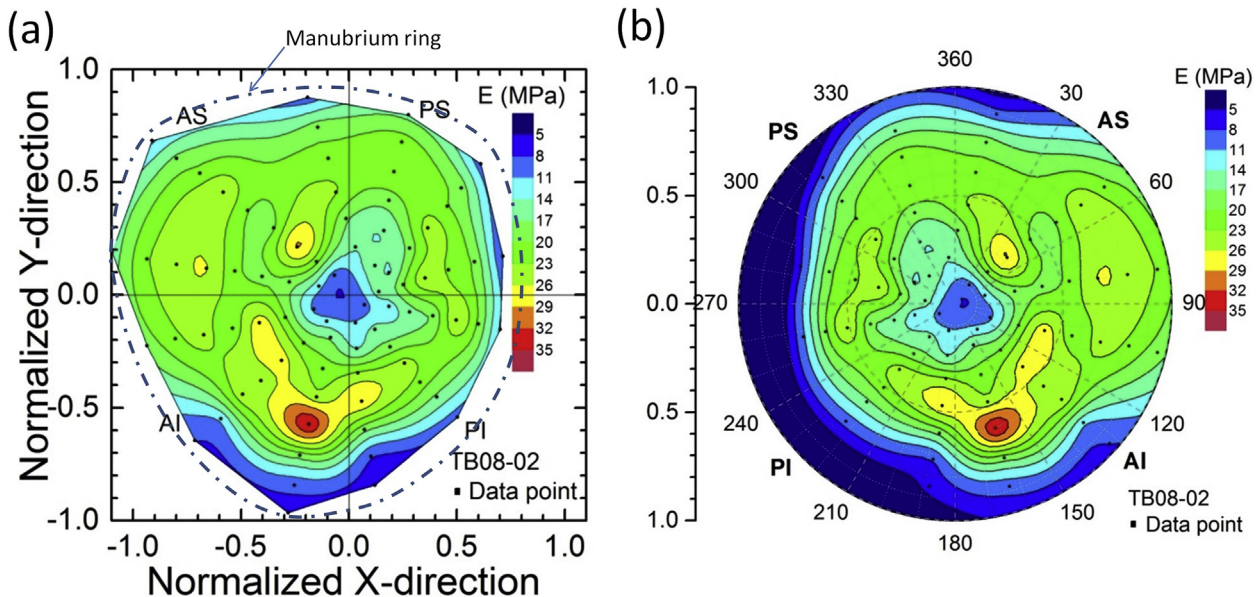


Fig. 5. Young's modulus distribution of TM (TB08-02) at the medial surface. An outline of the manubrium is plotted as a blue dot-dash curve in Fig. 5a. (a) Original Young's modulus map in normalized x - y coordinates; (b) Smoothed map in normalized polar coordinates. Note, the malleus is located at $x = 0$, $0 < y < 1$ in Fig. 5a, and $\theta = 0^\circ$ or 360° , $0 < r < 1$.

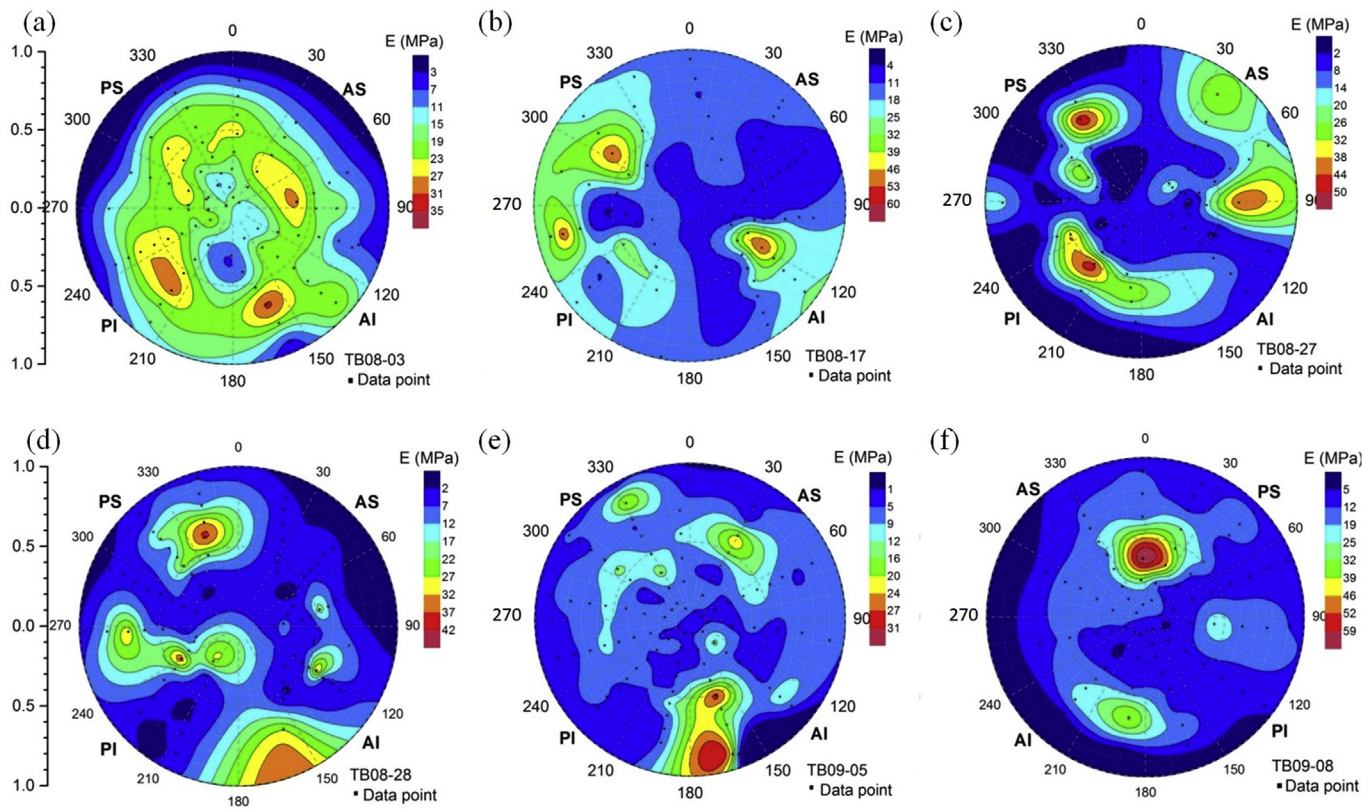


Fig. 6. Young's modulus map data at medial surface in normalized polar coordinates. (a). TB0803; (b). TB08-17; (c). TB08-27; (d). TB08-28; (e). TB 09-05; (f). TB09-08.

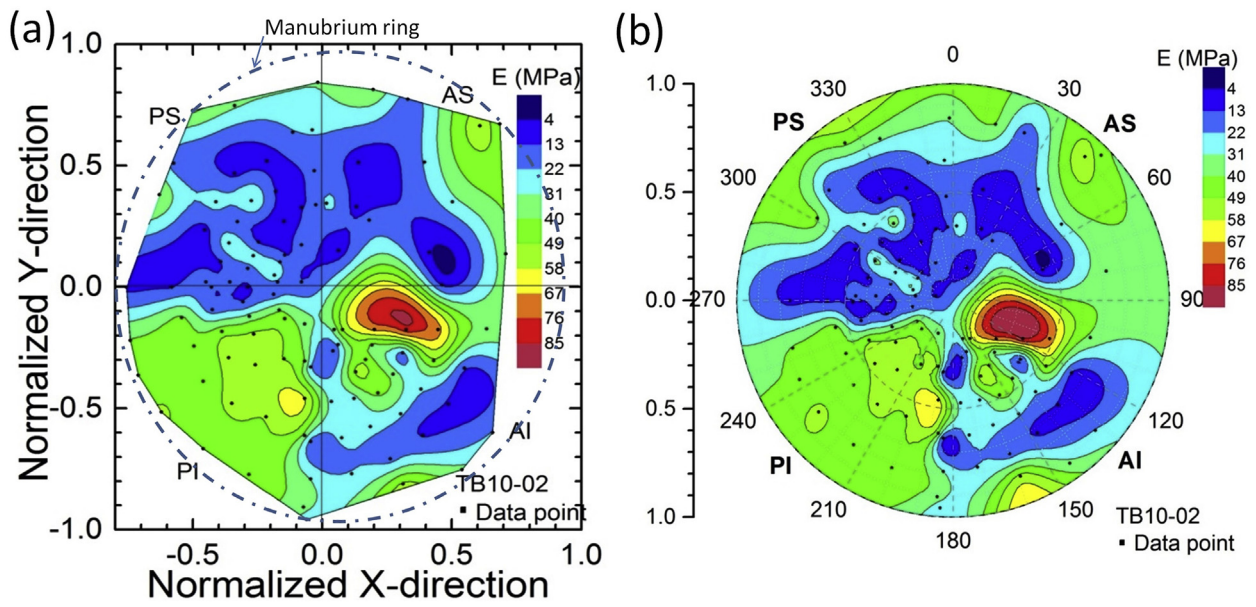


Fig. 7. Young's modulus distribution of TM (TB10-02) at the lateral surface. An outline of the manubrium is plotted as a blue dot-dash curve in Fig. 5a.(a). Original map in normalized x-y coordinates;(b). Smoothed map in normalized polar coordinates.

The Q-Q plot also provides an assessment of “goodness of fit” graphically. When a Q-Q plot shows an arc and “S” shape, it indicates that one of the distributions is more skewed relative to the other, indicating most likely the data follow a bimodal distribution (Kotz et al., 2005; Thode, 2002).

Figs. 9 and 10 show the normal Q-Q plot of the TM modulus data

for each of the four quadrants measured from the medial surface and the lateral surface, respectively. The points do not form one straight line. Fig. 11a and b include all the data points from the four quadrants. The points do not form a straight line even though most data within the range of P_{80} – P_{20} are close to a straight line. P_{80} and P_{20} are defined as the modulus at which 80% and 20% of the data

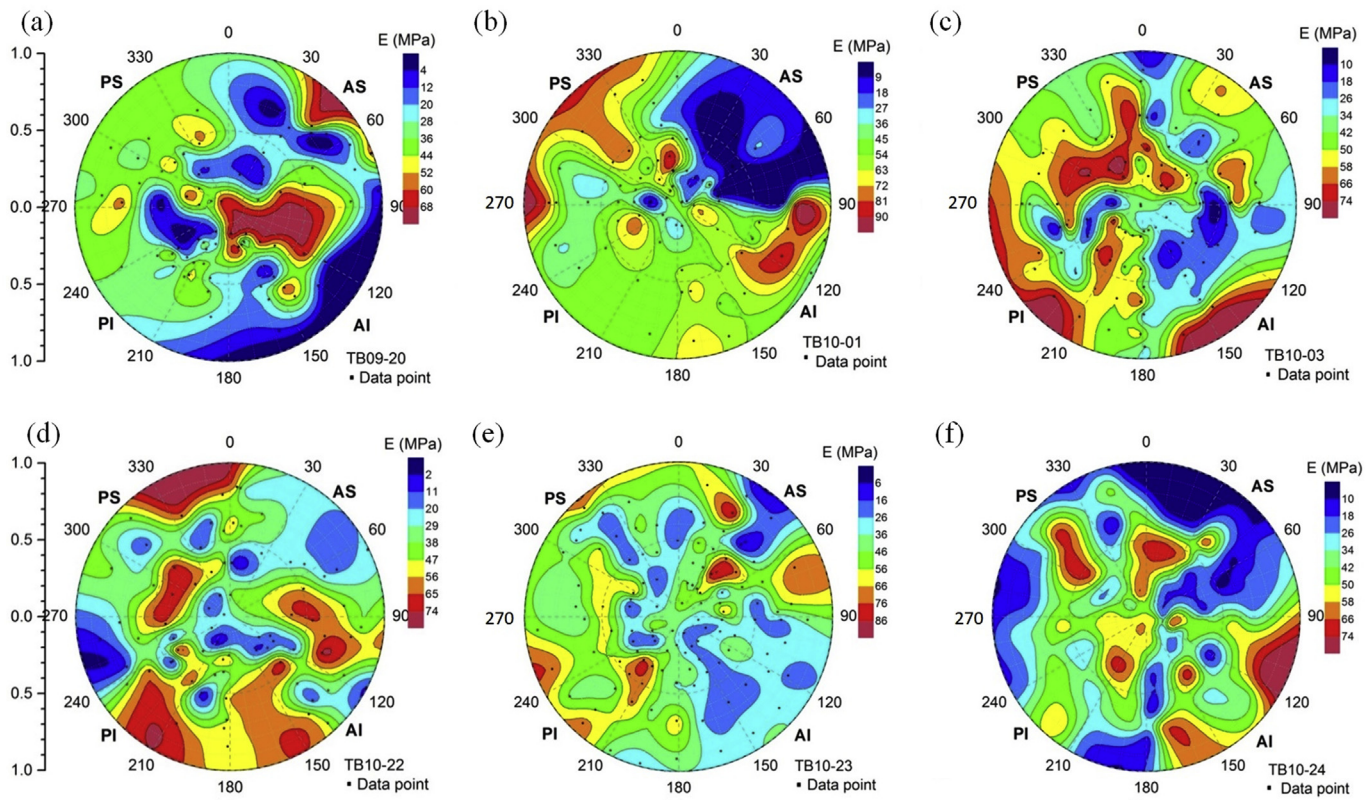


Fig. 8. Young's modulus map data of TMs at lateral surface in normalized polar coordinates. (a). TB09-20; (b). TB10-01; (c). TB10-03; (d). TB10-22; (e). TB10-23; (f) TB10-24.

points have these values, respectively. Based on Figs. 9–11, the data is likely to follow a bimodal distribution.

3.4. Bi-modal Gaussian distribution

In addition to the CDF distribution, the PDF distribution is also included. The modulus data points are combined from different TMs for the same quadrant of PS, AS, PI and AI. They are plotted in Fig. 12 for the 7 TMs with microindentation at the medial surface. Similarly, for the 8 TMs with microindentation at the lateral surface, the modulus data points are also combined from different TMs for the same quadrant of PS, AS, PI and AI. They are plotted in Fig. 13. Modulus data are also combined for the four quadrants. Fig. 14a and b shows the PDF histogram of all modulus values for the entire TM at the medial and lateral surfaces, respectively.

In general, the Young's modulus values of the human eardrum vary within 1.5–50 MPa for the medial surface, with most data falling within 5–30 MPa. The modulus values vary within 2–90 MPa for the lateral surface, and most data points are within the range of 15–60 MPa. The data on the AS quadrant show in general the smallest values compared with the other three quadrants.

Next, a bi-modal Gaussian CDF is used to fit the distribution parameters. Fig. 15a and b shows the experimental CDF curves of TM modulus data for all quadrants measured from the medial surface and lateral surface, respectively, as well as the best-fit results. The confidence level of the fitting is noted as COD (R^2), which is bounded between 0.0 and 1.0, corresponding to poor to excellent fitting, respectively. The fitting parameters and confidence levels obtained in this study are listed in Tables 4 and 5 for the medial surface and the lateral surface, respectively. All COD (R^2) range from 0.99 to 1.00, indicating an excellent fit for statistical analysis. The

standard deviations for all parameters are calculated through the Levenberg-Marquardt algorithm, which are summarized in Tables 4 and 5 following the \pm symbol. The relative standard deviation was mostly in the range of 2%–8%, up to 11%, which indicate excellent confidence levels and statistical reliability. It indicates that the Young's modulus can be well described using the bimodal Gaussian distribution and the Young's modulus maps can be most possibly modeled as a bi-variate Gaussian map. In Fig. 15, the bimodal Gaussian function fits the CDF well for TM modulus at both medial and lateral surfaces.

With these parameters known, the theoretical PDF curves, superimposed in Figs. 12–14, agree reasonably well with the corresponding histograms. In Fig. 12, two peaks are seen clearly that occur at 6–8 MPa and 19–20 MPa for all TM quadrants at the medial surface. The weight factor for two expectations is close to 50% for the PS, PI and AI quadrants while only 40% for the AS quadrant. For the entire TM at the medial surface, the two expectations are 6.6 MPa and 19.2 MPa with 0.5 wt ratio, as shown in Fig. 14a. Except for Fig. 13a, where two peaks overlap at 40 MPa, the other three quadrants (AS, PI, and AI) all show two peaks of modulus in the ranges of 12–24 MPa and 44–47 MPa as shown in Fig. 13. The weight factors for the PI and AI quadrants (0.22 and 0.37) are less than that of the AS quadrant (0.48). For the entire TM at the lateral surface, the modulus has two peaks at 16.3 MPa and 41.6 MPa with the weight ratio 18:82 as shown in Fig. 14b. This weight factor represents the ratio of two expectations. The differences in weight factors in different quadrants may be due to differences in the fiber distribution and density.

In the literature, the average values reported for the TM modulus are approximately 20 MPa (Von Békésy, 1960) and about 40 MPa (Kirikae, 1960) in the circumferential and radial directions, respectively. In this study, even smaller values of TM modulus were

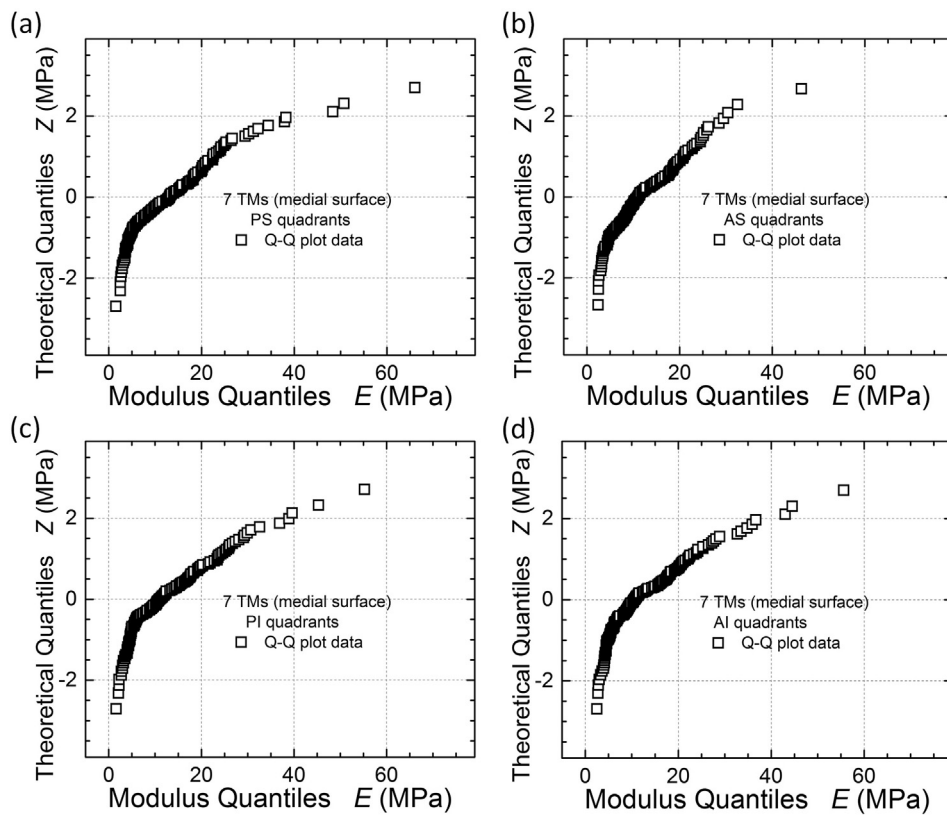


Fig. 9. Normal Q-Q plots of four quadrants for 7 TM at medial surfaces. (a). PS quadrant; (b). AS quadrant; (c). PI quadrant; (d). AI quadrant.

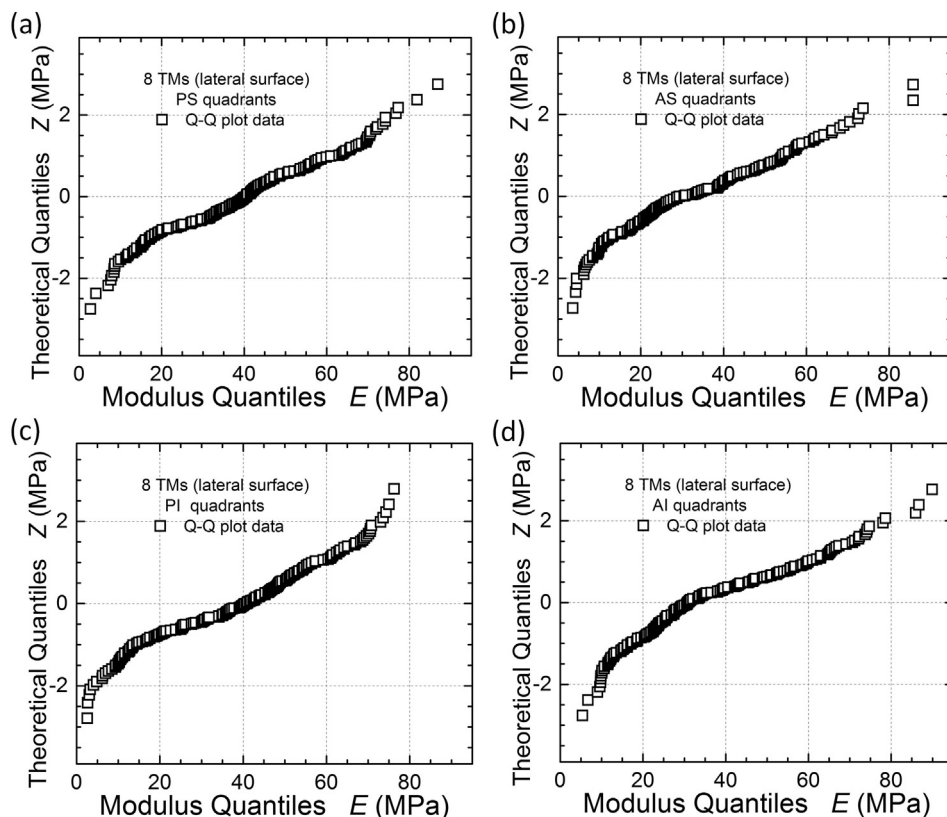


Fig. 10. Normal Q-Q plots of four quadrants of TM at the lateral surface. (a). PS quadrant; (b). AS quadrant; (c). PI quadrant; (d). AI quadrant.

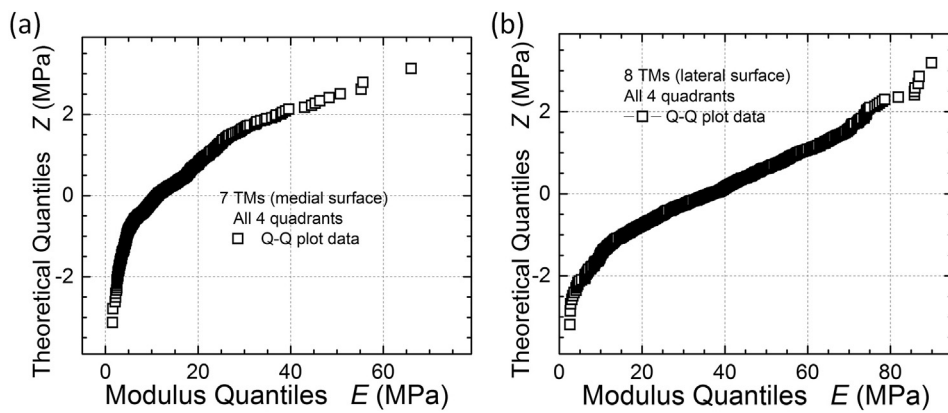


Fig. 11. Normal Q-Q plots for all quadrants.(a). 7 TM at the medial surface; (b). 8 TM at the lateral surface.

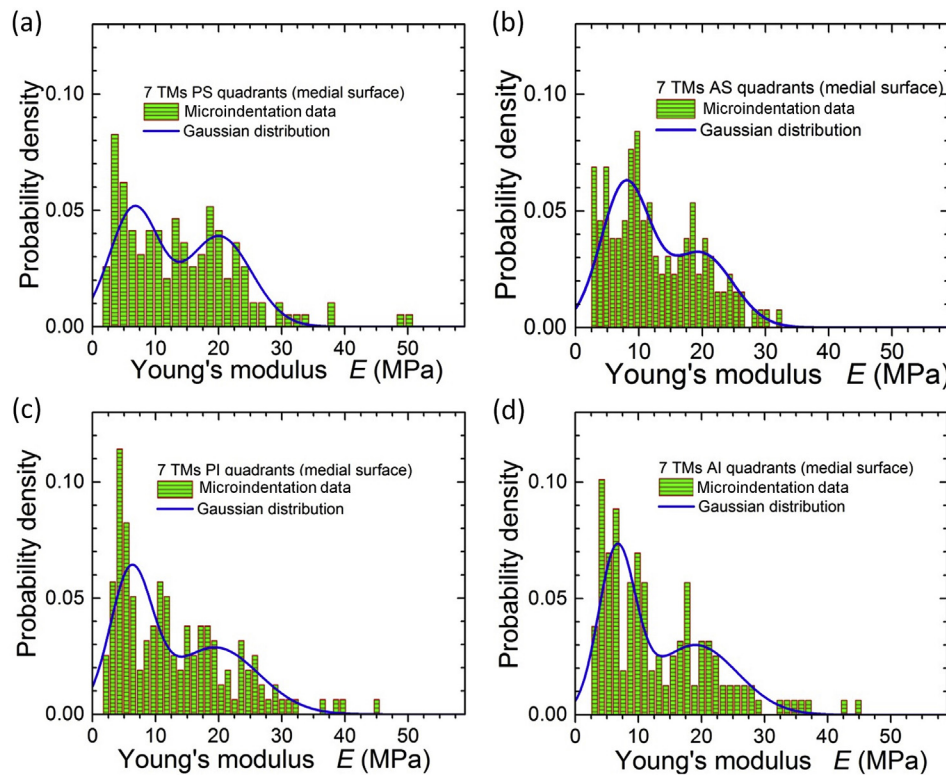


Fig. 12. Bi-modal Gaussian distribution of four quadrants for 7 TM at the medial surface.(a). PS quadrant; (b). AS quadrant; (c). PI quadrant; (d). AI quadrant.

obtained. They are 6.6 ± 3.5 MPa and 16.3 ± 7.1 MPa at both the medial and the lateral surfaces, respectively. The smaller TM modulus may be associated with lower density of collagen fibers. The larger modulus values measured as 19.2 ± 6.2 MPa and 41.6 ± 18.8 MPa for the circumferential and radial fiber layers, respectively, may be the consequence of difference in collagen fiber density. From Table 4, the two averages of the mean values (μ_{m1} and μ_{m2}) for the four quadrants at the medial surface are 19.6 ± 0.5 MPa and 6.8 ± 0.8 MPa, likely corresponding to the main circumferential fibers and the minor fibers such as transverse fibers, TIR (trigonum interradiale in Fig. 3) fibers and parabolic fibers (Fig. 3), respectively. The statistical average of the modulus of 19.6 MPa is very close to the value of 19.2 MPa obtained from all four quadrants. The value is consistent with the nearly 20 MPa reported for the TM in the circumferential direction (Table 1). From Table 5, the two

averages of the mean values (μ_{l2} and μ_{l1}) for the four quadrants at the lateral surface are 44.3 ± 3.1 MPa and 23.6 ± 11.8 MPa, likely corresponding to the main radial fibers and the minor fibers such as R_1 radial fibers, R_2 radial fibers, and SMR submucous fine radial fibers (Fig. 3), respectively. The average of the larger mean values (μ_{m2}), quoted as a representative modulus, of 44.3 MPa is consistent with most reported data for the modulus in the radial direction (Table 1). It is noted that the modulus values at minor radial fibers have a higher standard deviation than the other fibers, which may be due to the huge difference in configurations among the three minor radial fibers. Another factor could be the effect of the thickness of the TM. The thinnest part of the TM is found in the central region between the annulus and the manubrium (Kuypers et al., 2006) where there were no modulus measurements. The TM thickness has a significant effect on measurement of modulus

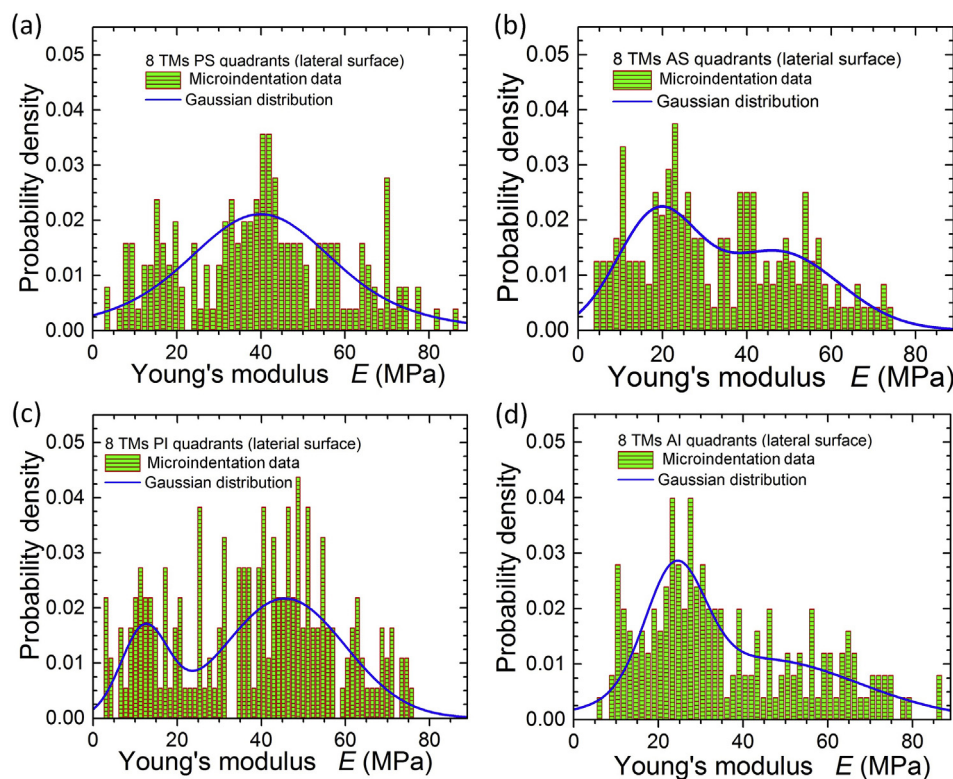


Fig. 13. Bi-modal Gaussian distribution of four quadrants for 8 TM at the lateral surface.(a). PS quadrant; (b). AS quadrant; (c). PI quadrant; (d). AI quadrant.

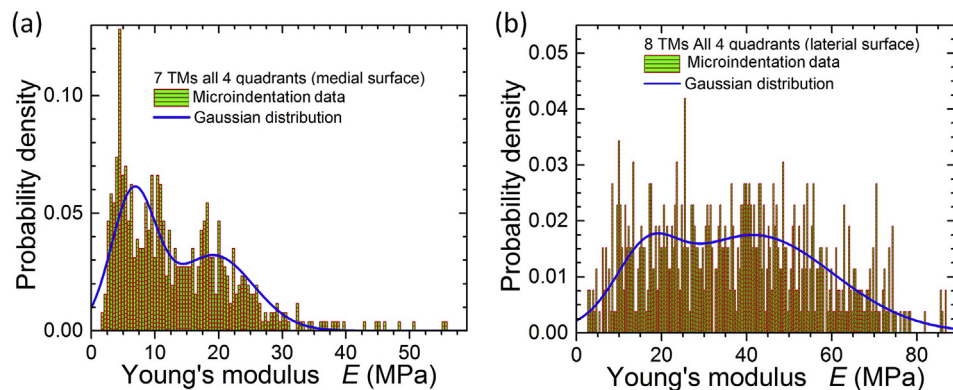


Fig. 14. Bi-modal Gaussian distribution of all quadrants.(a). 7 TM at the medial surface; (b). 8 TM at the lateral surface.

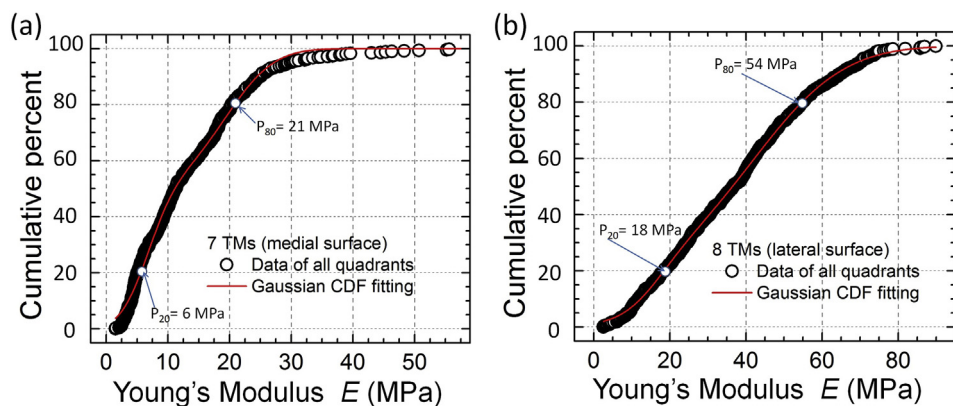


Fig. 15. Bi-modal Gaussian distribution CDF fitting of all quadrants. (a). 7 TM at the medial surface; (b). 8 TM at the lateral surface.

Table 4

Parameters for the bimodal Gaussian distribution at the medial surface.

Parameters	PS	AS	PI	AI	Whole
α_{m1}	0.50 ± 0.033	0.40 ± 0.035	0.50 ± 0.041	0.50 ± 0.038	0.50 ± 0.019
μ_{m1}	20.1 ± 0.479	19.8 ± 0.602	19.4 ± 0.998	19.0 ± 0.729	19.2 ± 0.329
σ_{m1}	5.13 ± 0.445	5.03 ± 0.465	6.93 ± 0.795	6.65 ± 0.063	6.22 ± 0.264
μ_{m2}	6.61 ± 0.332	7.85 ± 0.261	6.09 ± 0.264	6.56 ± 0.165	6.59 ± 0.117
σ_{m2}	3.94 ± 0.265	3.91 ± 0.163	3.34 ± 0.269	2.92 ± 0.177	3.49 ± 0.095
Data points	142	132	148	141	563
COD(R ²)	0.994	0.997	0.991	0.994	0.996

Note, the subscription "m" refers to the medial surface. α_{m1} is the weight factor of μ_{m1} .The standard errors of the parameters through Levenberg-Marquardt algorithm are shown following the \pm symbol.**Table 5**

Parameters for the bimodal Gaussian distribution at the lateral surface.

Parameters	PS	AS	PI	AI	Whole
α_{L1}	0.50 ± 0.057	0.482 ± 0.038	0.221 ± 0.006	0.368 ± 0.019	0.176 ± 0.011
μ_{L1}	39.8 ± 0.980	18.5 ± 0.636	12.2 ± 0.209	23.9 ± 0.199	16.3 ± 0.103
σ_{L1}	26.6 ± 1.96	9.47 ± 0.399	5.62 ± 0.286	6.95 ± 0.365	7.05 ± 0.287
μ_{L2}	40.0 ± 0.614	47.3 ± 1.430	45.7 ± 0.173	44.1 ± 0.758	41.6 ± 0.314
σ_{L2}	14.6 ± 1.49	14.5 ± 0.971	14.3 ± 0.181	23.2 ± 0.366	18.8 ± 0.188
Data points	171	158	189	177	695
COD(R ²)	0.994	0.998	0.999	0.998	0.999

Note, the subscription "L" refers to the lateral surface. α_{L1} is the weight factor of μ_{L1} .The standard errors of the parameters through Levenberg-Marquardt algorithm are shown following the \pm symbol.

through tensile experiments and simulation (Liang et al., 2015, 2016). In the tension of a TM strip, the thinnest region of the TM shows the smallest Young's modulus when the TM is assumed to have the uniform thickness. The underlying reasons for the existence of the two peaks in the TM modulus need further investigation to examine possible correlations between the TM microstructures and the modulus data.

3.5. Modeling the distribution of Young's modulus

The Young's modulus curves (Figs. 12–14) show one or more peaks, and the locations and values vary in individual TMs (Figs. 5–8). Moreover, individual TMs show variation in the modulus map. The statistical analysis indicates that the Young's modulus follows the bimodal Gaussian distribution. From individual TM modulus maps, it appears that the bivariate Gaussian surface or the summation of several different bivariate Gaussian surfaces is appropriate to model the Young's modulus map. Thus, all modulus values from different TMs are plotted in a single map, as in Fig. 16a for the medial surface from all 7 TM samples, and Fig. 17a for the lateral surface from all 8 TMs, respectively.

The bivariate Gaussian curves show a bell shape with multiple peaks. Thus, we consider describing the spatial distribution of the Young's modulus as a series of bivariate Gaussian functions in polar coordinates by:

$$E(r, \theta) = \sum_{i=1}^N A_i * e^{\left(-0.5 \left[\frac{(r-\mu_{ri})^2}{\sigma_{ri}^2} + \frac{(\theta-\mu_{\theta i})^2}{\sigma_{\theta i}^2}\right]\right)} + B \quad (15)$$

where N is the number of terms; A_i is the peak modulus; B is the baseline modulus; μ and σ are the expectation (mean) and standard deviation, respectively; the subscripts r and θ represent radial and angular coordinates, respectively, as shown in Fig. 1a. The best-fit parameters A_i , B , σ_i , and μ_i ($i = 1, \dots, N$) are determined using the nonlinear least squares Levenberg-Marquardt method.

It is seen in Figs. 16a and 17a that the combined modulus maps show numerous bell shapes. Under such a situation, it is

appropriate to use a series of bivariate Gaussian functions to model the modulus map. Since the modulus has more bell shapes with different peaks, two types of mapping functions are used: single bivariate Gaussian and bi-bivariate Gaussian. The bivariate Gaussian is a normal distribution function for the radial and the angular coordinates. It has a baseline modulus value B , and several peak moduli A_i . The best-fit parameters A_i , B , μ_{ri} , σ_{ri} , $\mu_{\theta i}$, and $\sigma_{\theta i}$ ($i = 1, \dots, N$) are listed in Table 6 for the two fitting approaches. The standard deviations for all parameters through the Levenberg-Marquardt algorithm are also summarized in Table 6. The confidence levels of modeling is much lower than the statistical analysis in (Tables 4 and 5), which indicates poor statistical reliability. From Table 6, the bi-bivariate Gaussian maps show better modeling than the single-bivariate Gaussian map. It is noted that, in theory, there are many parameter sets which can be fitted through nonlinear Levenberg-Marquardt algorithm. In practice, only one set of parameter is searched; the number of parameters depends on the initial values, the boundaries, and the parameter values. The parameters are 6 and 11 in the single- and bi-bivariate Gaussian functions, respectively. In addition to the initial values and the boundaries, more parameters result in difficulty in fitting through the nonlinear fitting algorithm. For a large number of parameters such as 21 parameters in the quad-bivariate Gaussian fitting, there are occasions when the algorithm does not lead to convergence even after 400 iterations. In consideration of a balance between accuracy and convergence in fitting, the bi-bivariate Gaussian function turns out to be the best option to describe the spatial distribution of Young's modulus.

As shown in Fig. 16b and c, the modulus distribution at the medial surface has a certain trend. At the perimeter of the eardrum close to the annulus ring, the Young's modulus is relatively small; it is considered to be the baseline modulus. This is reasonable since the TM tissue close to the annulus ring has a longer perimeter and is softer than the membrane in the central region. In the central region around the umbo, the Young's modulus is also smaller, possibly due to the fact that it is close to the umbo which provides support to the membrane. It is seen that, along a ray from the perimeter to the center, the Young's modulus follows a small-large-

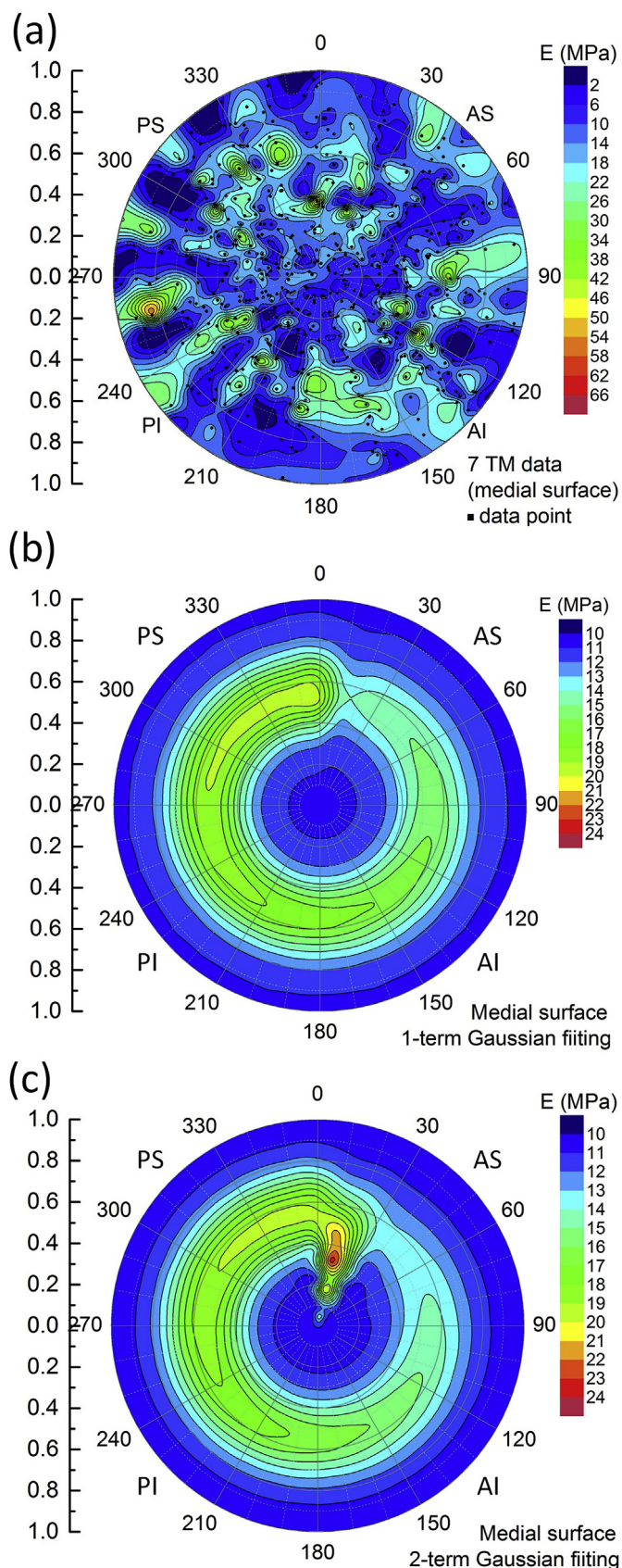


Fig. 16. Young's modulus map for 7 TM at the medial surface.(a). Combined experimental data from 7 TMs.(b). Single-bivariate Gaussian map.(c). Bi-bivariate Gaussian map.

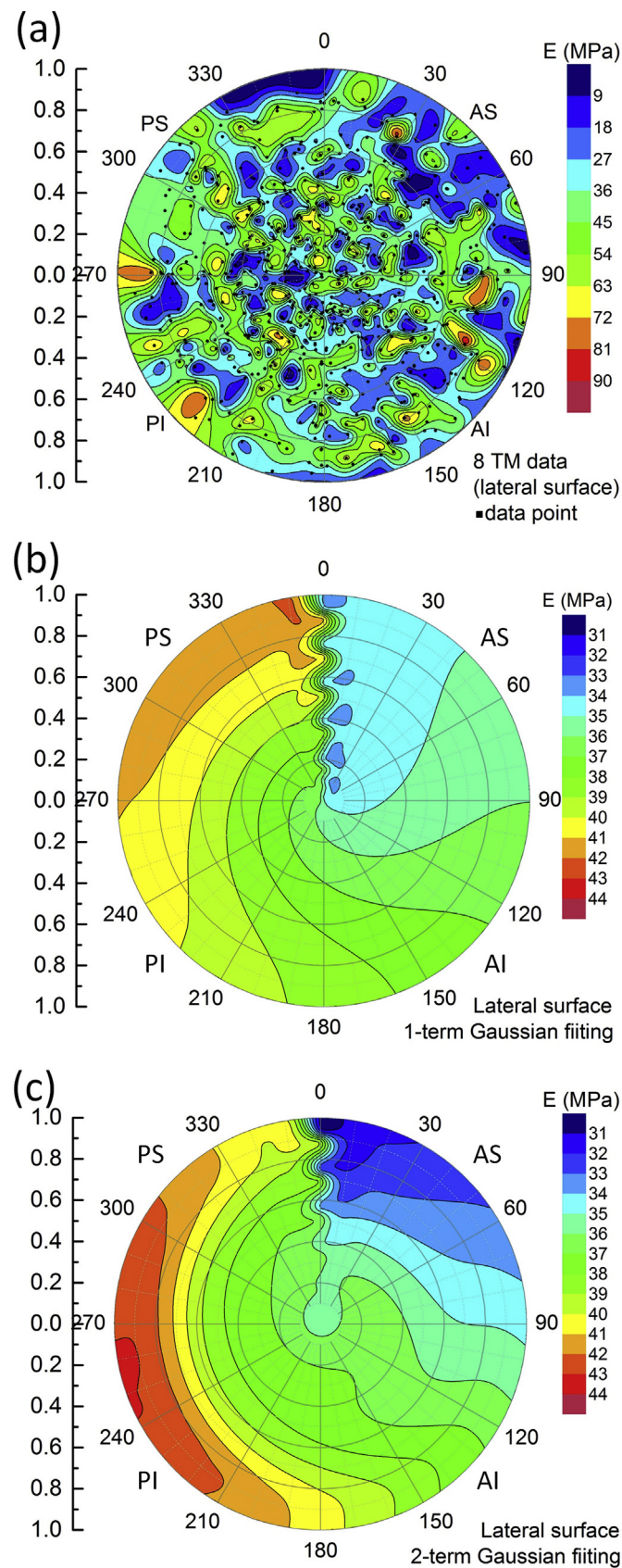


Fig. 17. Young's modulus map for 8 TM at the lateral surface(a). Combined experimental data from 8 TMs.(b). Single-bivariate Gaussian map.(c). Bi-bivariate Gaussian map.

Table 6

Parameters for the single- and bi-bivariate Gaussian maps.

Parameters	Single-bivariate Gaussian		Bi-bivariate Gaussian	
	Medial surface	Lateral surface	Medial surface	Lateral surface
A_1 (MPa)	8.66 \pm 2.76	8.00 \pm 4.05	12.8 \pm 5.86	6.44 \pm 5.10
A_2 (MPa)	N/A	N/A	8.96 \pm 2.87	12.6 \pm 7.70
B (MPa)	10.9 \pm 0.782	33.6 \pm 4.96	10.6 \pm 0.832	30.1 \pm 13.3
μ_{r1} (MPa)	0.546 \pm 0.020	1.00 \pm 0.49	0.300 \pm 0.123	0.206 \pm 0.108
μ_{r2} (MPa)	N/A	N/A	0.548 \pm 0.021	0.956 \pm 0.523
σ_{r1} (MPa)	0.130 \pm 0.028	0.684 \pm 0.340	0.192 \pm 0.115	0.321 \pm 0.182
σ_{r2} (MPa)	N/A	N/A	0.138 \pm 0.030	0.306 \pm 0.221
$\mu_{\theta1}$ (°)	360.0 \pm 79.0	325.4 \pm 72.7	12.0 \pm 3.75	180.0 \pm 32.9
$\mu_{\theta2}$ (°)	N/A	N/A	360.0 \pm 51.3	258.8 \pm 42.8
$\sigma_{\theta1}$ (°)	250.9 \pm 121	151.9 \pm 94.3	9.54 \pm 4.62	360.0 \pm 120.9
$\sigma_{\theta2}$ (°)	N/A	N/A	208.8 \pm 107.9	115.6 \pm 59.3
COD (R^2)	0.060	0.108	0.074	0.13

Note, N/A means that these parameters are not applicable for single-bivariate Gaussian fitting, they are for use in the bi-bivariate Gaussian fitting only. The standard deviations of the parameters through Levenberg-Marquardt algorithm are shown following the \pm symbol.

small trend at the medial surface for circumferential fibers. This lower modulus close to the perimeter may be due to the existence of the P and TIR fibers, which have lower densities than the circumferential fibers. The highest modulus close to the half of the radius may be due to T fibers which have possibly higher density than the circumferential fibers. The contour lines for the modulus are distributed along the circumferential fiber directions (Fig. 1c). In Fig. 16b and c for the two different terms, the difference appears only in the region close to the malleus bone at $\theta = 0$ –30°. Since malleus bone exists in the top radial direction at the medial surface of the TM, these differences do not represent the modulus of the membrane and, therefore, should be ignored. Thus, the single-bivariate Gaussian function (Fig. 16b) is sufficiently accurate to describe the map of Young's modulus for circumferential fibers.

As shown in Fig. 17b and c, the modulus distribution at the lateral surface has a different trend. The AS quadrant shows the smallest modulus distribution and the AI quadrant shows the smallest modulus. The lower modulus in the AS quadrant may be due to the fact that if SMR fibers exist, they probably have lower fiber density than the other straight R_1 radial fibers. However, the highest modulus is distributed close to the annulus ring edge at the PS and PI quadrants ($\theta = 200$ –300°); then the modulus decreases gradually along the radial direction to the origin at the umbo. The highest modulus at the edge between the PS and PI quadrant may be due to the presence of the R_2 fibers, which are radial fibers diverging or crossing over their annulus ring terminals, at which fibers have higher density than the other straight R_1 fibers in the radial direction. It appears that the modulus of the radial fibers is distributed in a strip shape along the radial fibers. The modulus increases gradually with the increase of polar angle, from the AS quadrant to AI quadrant. However, it changes the distribution along the circumferential direction. Around the region close to the malleus bone, the modulus has some perturbation since the malleus bone is attached to the other medial surface. Therefore, the bi-bivariate Gaussian (Fig. 17c) provides the best-fit to the modulus map of Young's modulus for the radial fibers.

It is noted that, for the modulus map, the confidence level for the coefficient of determination (COD) or R squared (R^2) is as low as 0.2–0.3. This value is not as high as 0.99 for the fitting of the CDF. Due to limited TM samples (7 TMs for the medial surface and 8 TMs for the lateral surface) and microindentation data points (about 600 and about 700 data points, respectively), the statistical analysis and the Young's modulus map may likely have some uncertainties and variation. However, the TM out-of-plane modulus distribution will perhaps improve the TM models for computational simulations of

sound transmission. The results obtained in this study will enable input of TM mechanical properties in both the in-plane and the out-of-plane directions, necessary for simulation of TM vibrations under sound pressure. With the mechanical properties, data reported herein and other data reported in the literature for the TM, in the future, the two-layer collagen fibers of the TM can be assigned with different material properties, to account for anisotropy and viscoelastic behavior for the entire TM, for simulations of sound transmission with improved accuracy.

4. Conclusion

Measurement of the Young's modulus in the through-thickness direction was made by spherical microindentation on a human TM. The out-of-plane Young's modulus was measured for 7 TMs on the medial surface and 8 TMs on the lateral surface, respectively. The collagen fiber layers are in direct contact with the nanoindenter tip in saline condition. Viscoelastic microindentation analysis yields the Young's relaxation modulus data, which is converted to the Young's modulus at a given strain rate. The modulus data exhibit strong variation from one location to another. The Young's modulus varies over a wide range from 1.5 MPa to 50 MPa (mostly around 5–30 MPa) on the medial surface, and 2 MPa–90 MPa (mostly around 15–60 MPa) on the lateral surface.

The Q-Q plot, and the empirical CDF and PDF histograms are used for statistical analysis. Using the normal Q-Q plot, the S-shaped curves indicate a bimodal Gaussian distribution for both the radial fibers on the lateral surface and the circumferential fibers on the medial surface. The distribution parameters are determined from the best-fit CDF for each quadrant and for the entire TM. The PDF agrees well with the histograms. The two means of Young's modulus are determined as 6.6 MPa and 19.2 MPa for the medial surface, and 16.3 MPa and 41.6 MPa for the lateral surface, respectively. The lower modulus is likely due to lower fiber density, while the higher modulus is close to the values reported in the literature.

The Young's modulus maps were also modeled as a series of bivariate Gaussian functions in polar coordinates at both the medial and lateral surfaces over the entire TM. Two types of bivariate Gaussian functions were considered: single and double series. The parameters for the spatial distribution of modulus were also determined from the best-fit. For the medial surface, Young's modulus changed mainly along the radial direction, and followed a small-large-small trend from the perimeter to the center. For the lateral surface, Young's modulus showed a trend different from the medial surface. The AS quadrant showed the smallest modulus, then followed by the AI quadrant. The higher modulus was located close to the annulus ring edge at the PS and PI quadrants. The modulus gradually decreased along the radial direction to the origin, which is set at the umbo. Among the three types of models, single-bivariate and bi-bivariate Gaussians provided the best-fit to the spatial distribution of Young's modulus at the medial surface and the lateral surface, respectively. The local properties measured by microindentation can be used as input for future computer simulations of the middle ear using accurate two-layer structures with different modulus values over the TM to understand sound transmission.

Acknowledgments

We acknowledge the support of DOD W81XWH-14-1-0228, NIH R01DC011585, DOD W81XWH-13-MOMJPC5-IPPEHA, and NSF CMMI-1636306, CMMI-1661246, and CMMI-172043. Lu acknowledges the Louis A. Beecherl Jr. Chair for additional support. We also thank Dr. Chengkai Dai at University of Oklahoma, Dr. Wei Li at Hough Ear Institute for assistance on sample preparations, and Dr.

Xuelin Wang at Huazhong University of Science and Technology for helpful discussions. The authors thank Dr. Dani Fadda and one of the anonymous reviewers for editing the manuscript.

References

Aernouts, J., Aerts, J.R.M., Dirckx, J.J., 2012. Mechanical properties of human tympanic membrane in the quasi-static regime from *in situ* point indentation measurements. *Hear. Res.* 290, 45–54.

Beyea, J.A., Rohani, S.A., Ladak, H.M., Agrawa, S.K., 2013. Laser Doppler vibrometry measurements of human cadaveric tympanic membrane vibration. *Otolaryngol. Head Neck Surg.* 142, 17–26.

Chambers, J.M., Cleveland, W.S., Kleiner, B., Tukey, P.A., 1983. Graphical Methods for Data Analysis. Wadsworth International Group, Duxbury Press.

Cheng, T., 2007. Mechanical Properties of Human Middle Ear Tissues. PhD dissertation, University of Oklahoma.

Cheng, T., Dai, C., Gan, R.Z., 2007. Viscoelastic properties of human tympanic membrane. *Ann. Biomed. Eng.* 35, 305–314.

Daphalapurkar, N.P., Dai, C., Gan, R.Z., Lu, H., 2009. Characterization of the linearly viscoelastic behavior of human tympanic membrane by nanoindentation. *J. Mech. Behav. Biomed. Mater.* 2, 82–92.

Decraemer, W.F., Maes, M.A., Vanhuyse, V.J., 1980. An elastic stress-strain relation for soft biological tissues based on a structural model. *J. Biomech.* 13, 463–468.

Dobrev, I., Furlong, C., Cheng, J.T., Rosowski, J.J., 2014. Acousto-mechanical Response of the Human TM Characterized by High-Speed Digital Holographic Methods. Springer Berlin, pp. 657–660. Fringe 2013.

Eiber, A., Schidhilen, W., 1996. Reconstruction of hearing by mechatronical devices. *Robot. Autonom. Syst.* 19, 199–204.

Fay, J., Puria, S., Decraemer, W.F., Steele, C., 2005. Three approaches for estimating the elastic modulus of the tympanic membrane. *J. Biomech.* 38, 1807–1815.

Ferris, P., Prendergast, P.J., 2000. Middle-ear dynamics before and after ossicular replacement. *J. Biomech.* 33, 581–590.

Filliben, J.J., 1975. The probability plot correlation coefficient test for normality. *Technometrics* 17 (1), 111–117.

Gaihede, M., Liao, D., Gregersen, H., 2007. In vivo areal modulus of elasticity estimation of the human tympanic membrane system: modeling of middle ear mechanical function in normal young and aged ears. *Phys. Med. Biol.* 52, 803–814.

Gan, R.Z., Feng, B., Sun, Q., 2004. Three dimensional finite modeling of human ear for sound transmission. *Ann. Biomed. Eng.* 32, 847–859.

Gan, R.Z., Sun, Q., Feng, B., Wood, M.W., 2006. Acoustic-structural coupled finite element analysis for sound transmission in human ear-pressure distributions. *Med. Eng. Phys.* 28, 395–404.

Gan, R.Z., Dai, C., Wang, X., Nakmali, D., Wood, M.W., 2010. A totally implantable hearing system—Design and function characterization in 3D computational model and temporal bones. *Hear. Res.* 263, 138–144.

Gnanadesikan, R., 1977. Methods for Statistical Analysis of Multivariate Observations, second ed. John Wiley & Sons.

Greif, D.D., Aernouts, J., Aerts, J., Cheng, J.T., Horwitz, R., Rosowski, J.J., Dirckx, J.J., 2014. Viscoelastic properties of the human tympanic membrane studied with stroboscopic holography and finite element modeling. *Hear. Res.* 312, 69–80.

Hesabgar, S.M., Marshall, H., Agrawal, S.K., Samani, A., Ladak, H.M., 2010. Measuring the quasi-static Young's modulus of the eardrum using an indentation technique. *Hear. Res.* 263, 168–176.

Huang, G., Lu, H., 2006. Measurement of Young's relaxation modulus using nano-indentation. *Mech. Time-Dependent Mater.* 10, 229–243.

Huang, G., Daphalapurkar, N.P., Gan, R.Z., Lu, H., 2008. A method for measuring linearly viscoelastic properties of human tympanic membrane using nano-indentation. *J. Biomech. Eng.-Trans. ASME* 130, 014501.

Jeugt, S.V.D., Dirckx, J.J., Aerts, J.R.M., Bradu, A., Podoleanu, A.G., Buytaert, J.A.N., 2013. Full-field thickness distribution of human tympanic membrane obtained with optical coherence tomography. *J. Assoc. Res. Otolaryngol.* 14, 483–494.

Kirikae, I., 1960. The Structure and Function of the Middle Ear. University of Tokyo Press, Tokyo.

Knauss, W.G., Emri, I., Lu, H., 2008. Mechanics of polymers: viscoelasticity. In: Sharpe, W.N. (Ed.), *Handbook of Experimental Solid Mechanics*. Springer, New York, pp. 49–95.

Kochkin, S., 2005. MarkeTrak VII: hearing loss population tops 31 million people. *Hear. Rev.* 12, 16–29.

Kotz, S., Read, C.B., Balakrishnan, N., Vidakovic, B., 2005. *Encyclopedia of Statistical Sciences*. John Wiley & Sons, Inc, New York.

Kuypers, L.C., Decraemer, W.F., Dirckx, J.J., 2006. Thickness distribution of fresh and preserved human eardrums measured with confocal microscopy. *Otol. Neurotol.* 27, 256–264.

Lee, W.H., Radok, J.R.M., 1960. The contact problem for viscoelastic bodies. *J. Appl. Mech.* 27, 438–444.

Liang, J., Fu, B., Luo, H., Nakmali, D., Gan, R.Z., Lu, H., 2015. Characterisation of the nonlinear elastic behaviour of Guinea pig tympanic membrane using micro-fringe projection. *Int. J. Exp. Comput. Biomed.* 3 (4), 319–344.

Liang, J., Luo, H., Yokell, Z., Nakmali, D., Gan, R.Z., Lu, H., 2016. Characterization of the nonlinear elastic behavior of chinchilla tympanic membrane using micro-fringe projection. *Hear. Res.* 339, 1–11.

Lim, D.J., 1970. Human tympanic membrane: an ultrastructural observation. *Acta Otolaryngol.* 70 (3), 176–186.

Lim, D.J., 1995. Structure and function of the tympanic membrane: a review. *Acta Oto-Rhino-Laryngol. Belg.* 49, 101–115.

Lu, H., Wang, B., Ma, J., Huang, G., Viswanathan, H., 2003. Measurement of creep compliance of solid polymers by nanoindentation. *Mech. Time-Dependent Mater.* 7, 189–207.

Lu, H., Huang, G., Wang, B., Mamedov, A., Gupta, S., 2006. Characterization of the linear viscoelastic behavior of single-wall carbon nanotube/polyelectrolyte multilayer nanocomposite film using nanoindentation. *Thin Solid Films* 500, 197–202.

Lu, H., Lu, H., Dai, C., Gan, R.Z., 2009a. A comparison of Young's modulus for normal and diseased human eardrum at high strain rates. *Int. J. Exp. Comput. Biomed.* 1, 1–22.

Lu, H., Dai, C., Gan, R.Z., Lu, H., 2009b. Measurement of Young's modulus of human tympanic membrane at high strain rates. *J. Biomech. Eng.-Trans. ASME* 131, 064501.

Lu, H., Zhang, Y., Wang, B., Lu, H., 2010. Characterization of the compressive behavior of glass fiber reinforced polyurethane foam at different strain rates. *J. Offshore Mech. Arct. Eng.-Trans. ASME* 132 (2), 021301.

Lu, H., Lu, G., Roy, S., Lu, H., 2013. Characterization of the viscoelastic behavior of bismaleimide resin before and after exposure to high temperatures. *Mech. Time-Dependent Mater.* 17 (3), 369–399.

Lu, H., Du, Y., Hu, Z., Cooper, W.L., Lu, H., 2015. High-strain rate compressive behavior of glass beads under confinement. *Exp. Mech.* 55, 935–950.

Moller, P., 1981. Tympanosclerosis of the ear drum: a scanning electron microscopic study. *Acta Otolaryngol.* 91, 215–221.

Moller, P., 1984. Tympanosclerosis of the ear drum in secretory otitis media. *Acta Otolaryngol (Stockh) Suppl.* 414, 171–177.

Mota, C., Danti, S., D'Alessandro, D., Trombi, L., Ricci, C., Puppi, D., Dinucci, D., Milazzo, M., Stefanini, C., Chiellini, F., Moroni, L., Berrettini, S., 2015. Multiscale fabrication of biomimetic scaffolds for tympanic membrane tissue engineering. *Biofabrication* 7, 025005.

Puria, S., 2003. Measurement of human middle ear forward and reverse acoustics: implications for otoacoustic emissions. *J. Acoust. Soc. Am.* 113, 2773–2789.

Rosowski, J.J., Dobrev, I., Khaleghi, M., Lu, W., Cheng, J.T., Harrington, E., Furlong, C., 2013. Measurements of three-dimensional shape and sound-induced motion of the chinchilla tympanic membrane. *Hear. Res.* 301, 44–52.

Thode, H.C., 2002. Testing for Normality. CRC Press.

Von Békésy, G., 1960. Experiments in Hearing. McGraw Hill, New York.

Wang, X., Cheng, T., Gan, R.Z., 2007. Finite-element analysis of middle-ear pressure effects on static and dynamic behavior of human ear. *J. Acoust. Soc. Am.* 122, 906–917.

Xu, T., Du, Y., Luo, H., Hu, Z., Wang, X., Guo, L., Lu, H., 2018. Characterization of the mechanical behavior of Colorado Mason sand at grain-level by nano-indentation. *Exp. Mech.* 58 (3), 449–463.

Zhang, X., Gan, R.Z., 2010. Dynamic properties of human tympanic membrane—experimental measurement and modelling analysis. *Int. J. Exp. Comput. Biomed.* 1, 252–270.

Zhang, X., Gan, R.Z., 2013. Dynamic properties of human tympanic membrane based on frequency-temperature superposition. *Ann. Biomed. Eng.* 41, 205–214.